1   **Revision 3**

2   **Compressional behavior and spin state of δ-(Al,Fe) OOH at high pressures**

3

4   **Itaru Ohira[1,a*], Jennifer M. Jackson[2], Natalia V. Solomatova[2,b], Wolfgang**

5   **Sturhahn[2], Gregory J. Finkelstein[2,c], Seiji Kamada[1,3], Takaaki Kawazoe[4,5], Fumiya**

6   **Maeda[1], Naohisa Hirao[6], Satoshi Nakano[7], Thomas S. Toellner[8], Akio Suzuki[1], Eiji**

7   **Ohtani[1]**

8   [1] Department of Earth Science, Graduate School of Science, Tohoku University, Sendai

9   980-8578, Japan

10   [2] Seismological Laboratory, California Institute of Technology, Pasadena, California

11   91125, U.S.A.

12   [3] Frontier Research Institute for Interdisciplinary Sciences, Tohoku University, Sendai

13   980-8578, Japan

14   [4] Bayerisches Geoinstitut, University of Bayreuth, Bayreuth, 95440 Germany

15   [5] Department of Earth and Planetary Systems Science, Graduate School of Science,

16   Hiroshima University, Higashi-Hiroshima 739-8526, Japan

17   [6] Japan Synchrotron Radiation Research Institute (JASRI), Hyogo, 679-5198, Japan

18   [7] National Institute for Materials Science (NIMS), Tsukuba 305-0044, Japan

19   [8] Advanced Photon Source, Argonne National Laboratory, Argonne, Illinois 60439, USA

20   [a] Present address: HPCAT, Geophysical Laboratory, Carnegie Institution of Washington,

21   Argonne, Illinois 60439, U.S.A.

22   [b] Present address: Laboratoire de Géologie de Lyon, Ecole Normale Supérieure de Lyon,

23   Université Claude Bernard Lyon 1, CNRS UMR 5276, Lyon, France

1

24   ^{c} Present address: Hawaii Institute of Geophysics and Planetology, School of Ocean and

25   Earth Sciences, University of Hawaii at Manoa, Honolulu, Hawaii 96822, U.S.A.

26   * *Corresponding author: itaru.ohira@gmail.com*

27

28   **ABSTRACT**

29   Hydrogen transport from the surface to the deep interior and distribution in the mantle

30   are important in the evolution and dynamics of the Earth. An aluminum oxy-hydroxide,

31   δ-AlOOH, likely influences the hydrogen transport process in the deep mantle because of

32   its high stability extending to lower mantle conditions. The compressional behavior and

33   spin states of δ-$(Al,Fe^{3+})OOH$ phases were investigated with synchrotron X-ray

34   diffraction and Mössbauer spectroscopy under high pressure and room temperature.

35   Pressure-volume (*P-V*) profiles of the δ-$(Al_{0.908(9)}{}^{57}Fe_{0.045(1)})OOH_{1.14(3)}$ (Fe/(Al+Fe) =

36   0.047(10), δ-Fe5) and the δ-$(Al_{0.832(5)}{}^{57}Fe_{0.117(1)})OOH_{1.15(3)}$ (Fe/(Al+Fe) = 0.123(2), δ-

37   Fe12) show that these hydrous phases undergo two distinct structural transitions

38   involving changes in hydrogen bonding environments and a high- to low-spin crossover

39   in Fe^{3+}. A change of axial compressibility accompanied by a transition from ordered-

40   ($P2_1nm$) to disordered-hydrogen bond (*Pnnm*) occurs near 10 GPa for both δ-Fe5 and δ-

41   Fe12 samples. Through this transition, the crystallographic *a* and *b* axes become stiffer,

42   whereas the *c* axis does not show such a change, as observed in pure δ-AlOOH. A

43   volume collapse due to a transition from high- to low-spin states in the Fe^{3+} ions is

44   complete below 32–40 GPa in δ-Fe5 and δ-Fe12, which is ~10 GPa lower than that

45   reported for pure ε-FeOOH. Evaluation of the Mössbauer spectra of δ-

46    $(Al_{0.824(10)}{}^{57}Fe_{0.126(4)})OOH_{1.15(4)}$ (Fe/(Al+Fe) = 0.133(3), δ-Fe13) also indicate a spin

47   transition between 32–45 GPa. Phases in the δ-(Al,Fe)OOH solid solution with similar

48   iron concentrations as those studied here could cause an anomalously high ρ/v_Φ ratio

49   (bulk sound velocity, defined as $\sqrt{K/\rho}$) at depths corresponding to the spin crossover

50   region (~900 to ~1000 km depth), whereas outside the spin crossover region a low ρ/v_Φ

51   anomaly would be expected. These results suggest that δ-(Al,Fe)OOH solid solution may

52   be important in understanding the heterogeneous structure of the deep Earth.

53

54   **Keywords**: δ-AlOOH, δ-(Al,Fe)OOH, hydrous mineral, high-pressure, X-ray diffraction,

55   Mössbauer spectroscopy, diamond anvil cell, synchrotron, water transport in the deep

56   mantle

57

58   **INTRODUCTION**
59
60   Volatile transport, in particular hydrogen in the forms of water and hydroxyl, from the

61   surface to the deep interior and distribution in the mantle are important in understanding

62   the evolution and dynamics of the Earth. Important hosts of hydrogen in the deep mantle

63   are hydrous and nominally-anhydrous minerals (e.g., Bell and Rossman 1992; Smyth and

64   Jacobsen 2006; Ohtani 2005, 2015, Ohtani et al. 2016; Wirth et al. 2007; Pearson et al.

65   2014; Kaminsky 2017; Tschauner et al. 2018). A dense aluminum oxy-hydroxide, δ-

66   AlOOH, likely plays a key role in hydrogen transport in the mantle transition zone and

67   the lower mantle (e.g., Ohtani et al. 2016). This hydrous phase is a high-pressure

68   polymorph of diaspore (α-AlOOH) and boehmite (γ-AlOOH), and was first synthesized

69   by Suzuki et al. (2000) at 21 GPa and 1273 K in a multi-anvil apparatus. High pressure

70   and high temperature experiments using a multi-anvil apparatus and a laser heated

3

71   diamond anvil cell (DAC) combined with in situ X-ray diffraction (XRD) have

72   demonstrated the stability of δ-AlOOH at 21–142 GPa and 973–2410 K, corresponding to

73   the conditions of the regions deeper than the lower transition zone (Sano et al. 2004,

74   2008; Pamato et al. 2015; Fukuyama et al. 2017; Abe et al. 2018; Duan et al. 2018). This

75   high stability implies that δ-AlOOH has the potential to transport hydrogen to the core-

76   mantle boundary (CMB) region.

77   The structure and physical properties of δ-AlOOH at ambient and high pressure

78   conditions have also been investigated. At ambient conditions, δ-AlOOH has a distorted

79   rutile-type structure with ordered (asymmetric) hydrogen bond ($P2_1nm$, off-centered

80   hydrogen positions termed "HOC-I") (Suzuki et al. 2000; Komatsu et al. 2006; Sano-

81   Furukawa et al. 2009; Kuribayashi et al. 2014; Xue and Kanzaki 2007). During

82   compression, the O···O distance (d_{OO}) of δ-AlOOH decreases, and this phase transforms

83   from HOC-I to a proton-disordered symmetric structure characterized by proton

84   tunneling ($Pnnm$, HOC-III) when the d_{OO} reaches the critical distance (2.439(6) Å) at 8

85   GPa (Kuribayashi et al. 2014). High-pressure powder and single-crystal XRD

86   measurements showed that this transition involves changes in axial compressibility

87   (Sano-Furukawa et al. 2009; Kuribayashi et al. 2014), which are also supported by the

88   recent computational studies (Cortona 2017; Kang et al. 2017; Pillai et al. 2018).

89   Further compression decreases the d_{OO}, and δ-AlOOH adopts a proton-centered

90   structure in which the d_{OO} is below ~2.366 Å ($Pnnm$, HC) (Tsuchiya and Tsuchiya 2009).

91   In our paper, the term of symmetrization indicates the transition to a proton-centered

92   structure (i.e. the transition from HOC-III to HC). Because this symmetrization may

93   cause a further increase in the bulk modulus, the determination of this transition pressure

4

94   is important to discuss the effect of δ-phase on the seismic velocity in the lower mantle.

95   However, computational studies using different approximations have shown conflicting

96   pressure conditions for the symmetrization of δ-AlOOH, ranging from 0 to 50 GPa

97   (Cortona 2017; Panero and Stixrude 2004; Tsuchiya and Tsuchiya 2009; Tsuchiya et al.

98   2002; Li et al. 2006; Cedillo et al. 2016; Bronstein et al. 2017; Kang et al. 2017; Pillai et

99   al. 2018). On the other hand, sound wave velocity measurements using Brillouin

100   spectroscopy demonstrated a precipitous increase by ~14% in the sound velocities of δ-

101   AlOOH from 6 to 15 GPa (Mashino et al. 2016), and Raman spectroscopy results showed

102   that the B_2 mode peaks of $P2_1nm$ broaden and disappear and the new peaks assigned to

103   the A_g mode of *Pnnm* appear above 5.6 GPa (Mashino et al. 2016). Infrared spectra

104   obtained from δ-AlOOH also demonstrated the change of pressure dependence of

105   hydrogen-based vibrational modes at 10 GPa (Kagi et al. 2010). The pressure conditions

106   of symmetrization determined from the spectroscopic measurements are in the pressure

107   range where changes in axial compressibility due to the occurrence of the order-disorder

108   ($P2_1nm$ HOC-I to *Pnnm* HOC-III) transition (Sano-Furukawa et al. 2009; Kuribayashi et

109   al. 2014). Although the pressure conditions of hydrogen bond symmetrization remains

110   unclear from the computational studies, the experimental data suggest that it would be

111   completed at shallow lower mantle pressures (Sano-Furukawa et al. 2009; Kuribayashi et

112   al. 2014; Mashino et al. 2016; Kagi et al. 2010). The recent neutron diffraction (ND)

113   study on δ-AlOOH by Sano-Furukawa et al. (2018) observed the order–disorder

114   transition of the hydrogen bond at 9.0 GPa and the symmtrization at 18.1 GPa, and

115   concluded that the discrepancy of symmtrization pressure between the experimental and

5

116   several computational studies is due to quantum and temperature effects, which was also

117   suggested in the computational studies by Bronstein et al. (2017).

118   δ-AlOOH forms a solid solution with hydrous $MgSiO_4H_2$ Phase H and ε-FeOOH (a

119   polymorph of goethite (α-FeOOH)) phases because they also have $P2_1nm$ and *Pnnm*

120   structures. Phase H has a proton-disordered symmetric structure (*Pnnm*, HOC-III) even at

121   ambient conditions (Bindi et al. 2014), and it transforms to a proton-centered structure

122   (*Pnnm*, HC) at around 30 GPa (Tsuchiya and Mookherjee 2015; Nishi et al. 2018). ε-

123   FeOOH phase has a proton-ordered asymmetric structure ($P2_1nm$, HOC-I) at ambient

124   conditions (Pernet et al. 1975). Density functional theory (DFT) calculations on ε-

125   FeOOH predicted that hydrogen bond symmetrization (i.e., the transition to HC-structure)

126   occurs at ~10 GPa (Thompson et al. 2017) or ~43 GPa (Gleason et al. 2013), and the

127   high-spin to low-spin (HS–LS) spin transition occurs at 56.5 GPa (Otte et al. 2009) or

128   64.8 GPa (Gleason et al. 2013). Hydrogen symmetrization pressure in ε-FeOOH is higher

129   than that in δ-AlOOH predicted from DFT calculations (~30 GPa; Tsuchiya and Tsuchiya

130   2009). However, it should be noted that the possible occurrence of a proton-disordered

131   symmetric structure (HOC-III), which could appear at pressures lower than a proton-

132   centered structure (HC), has not been evaluated in ε-FeOOH. The HS–LS transition

133   pressures in ε-FeOOH predicted by theory are close to those determined with X-ray

134   emission spectroscopy (40–60 GPa) and estimated from the volume collapse (~46–54

135   GPa) measured with XRD (Gleason et al. 2013).

136   The stability of hydrous δ-phase–ε-FeOOH–Phase H solid solution has been confirmed

137   up to at least 128 GPa and 2190 K in the $MgO–Al_2O_3–SiO_2–H_2O$ system (Ohira et al.

138   2014; Walter et al. 2015). Ohira et al. (2014) reported the coexistence of bridgmanite

139   with minor Al (MgSiO$_3$–6 mol% Al$_2$O$_3$) and Al-rich δ-phase–Phase H solid solution

140   containing about 40 mol% of a phase H component at 68 GPa and 2010 K. At 128 GPa

141   and 2190 K, hydrous δ–H solid solution coexisting with post-perovskite with minor Al

142   (MgSiO$_3$–5 mol% Al$_2$O$_3$) contains only 20 mol% of hydrous Phase H component (Ohira

143   et al. 2014). A recent experimental study has shown a continuous chain of hydrous phases

144   in cold oceanic crusts subducted from the Earth's surface to the top of the lower mantle

145   (Liu et al. 2019). In the hydrous basalt system, ε-phase is formed as ε-FeOOH–TiO$_2$ solid

146   solution (Liu et al. 2019; Okamoto and Maruyama 2004), which is stable at 8–17 GPa

147   and the cold slab temperatures (Liu et al. 2019; Okamoto and Maruyama 2004; Nishihara

148   and Matsukage 2016). Then, the hydrous δ-AlOOH–ε-FeOOH–phase H solid solution

149   (referred to as "Al-rich Phase H" in Liu et al. 2019) is formed, and it coexists with

150   bridgmanite, CaSiO$_3$-perovskite, stishovite, ferropericlase, and fluid at 25–26 GPa and

151   1273–1473 K, comparable to the condition of cold slabs at the top of the lower mantle

152   (Liu et al. 2019).

153   The composition of this hydrous phase formed in the hydrous basalt system is

154   ~Mg$_{0.11}$Si$_{0.20}$Al$_{0.63}$Fe$_{0.03}$O$_2$H, (Liu et al. 2019), which is close to AlOOH end-member.

155   Although the incorporation of ε-FeOOH is limited, it might influence the physical

156   properties of hydrous solid solution because Fe has large mass and might undergo the

157   spin transition at lower mantle pressures. Therefore, the physical properties of δ-AlOOH–

158   ε-FeOOH (δ-(Al,Fe)OOH) solid solution are important to understand the behavior of this

159   hydrous solid solution under lower mantle conditions. However, the physical properties

160   of δ-(Al,Fe)OOH under lower mantle conditions have not been examined. To address

7

161 these issues, we have conducted a set of high-pressure XRD and synchrotron Mössbauer

162 spectroscopy (SMS) experiments for δ-(Al,Fe)OOH.

163

EXPERIMENTAL METHODS

165
166 **δ-(Al,Fe)OOH crystals**

167 The samples are selected from aggregates of single crystals of δ-(Al,Fe)OOH phases

168 synthesized with a hydrothermal method using a 1000-ton Kawai-type multi anvil

169 apparatus installed at Bayerisches Geoinstitut, University of Bayreuth. The details of the

170 synthesis and characterization of δ-(Al,Fe)OOH under ambient conditions have been

171 reported by Kawazoe et al. (2017). Therefore, we provide only a brief description here.

172 The single crystals of δ-(Al,^{57}Fe)OOH were synthesized at 21 GPa and 1470 K from a

173 mixture of reagent-grade $Al(OH)_3$ (Rare Metallic Co., Ltd.) and Fe_2O_3 (96.64% ^{57}Fe,

174 ISOFLEX) using a Kawai-type multi-anvil apparatus. The initial dimensions of the

175 recovered crystals were in the range of 0.1–0.5 mm. The chemical compositions and

176 homogeneity of the δ-(Al,Fe)OOH crystals were confirmed using an electron microprobe

177 operating at 15 kV and 10 nA in the wavelength-dispersive mode (JEOL, JXA-8800,

178 installed at Tohoku University). The oxide mass deficits of the synthesized samples were

179 2–3 wt% greater than H_2O contents which would be expected based on the H_2O contents

180 in their ideal chemical formulas, suggesting the incorporation of additional water

181 (Kawazoe et al. 2017). In this study, δ-$(Al_{0.908(9)}{}^{57}Fe_{0.045(1)})OOH_{1.14(3)}$ (Fe/(Al+Fe) =

182 0.047(10)) synthesized and δ-$(Al_{0.832(5)}{}^{57}Fe_{0.117(1)})OOH_{1.15(3)}$ (Fe/(Al+Fe) = 0.123(2)) were

183 investigated with synchrotron XRD, and δ-$(Al_{0.824(10)}{}^{57}Fe_{0.126(4)})OOH_{1.15(4)}$ (Fe/(Al+Fe) =

184 0.133(3)) with synchrotron Mössbauer spectroscopy (SMS) experiments. Hereafter, the

8

185   three samples are referred to as δ-Fe5, δ-Fe12, and δ-Fe13, respectively. While δ-Fe5 was

186   selected from the crystals synthesized in the run H4473 in Kawazoe et al. (2017), δ-Fe12

187   and δ-Fe13 were from the crystals synthesized in the run H4468 in that study. The

188   additional sample for the single crystal XRD measurement at ambient conditions (δ-

189    $(Al_{0.807(7)}{}^{57}Fe_{0.117(4)})OOH_{1.15(3)}$ (Fe/(Al+Fe) = 0.127(3), identical ratio to δ-Fe12 within

190   error) was also from the run H4468 (Kawazoe et al. 2017). The Fe/(Al+Fe) ratios for the

191   Fe-poor sample (δ-Fe5) and the Fe-rich samples (δ-Fe12 and δ-Fe13) are identical to or

192   slightly higher than that of δ-phase formed at 25–26 GPa and 1273–1473 K in a hydrous

193   oceanic crust ($\sim Mg_{0.11}Si_{0.20}Al_{0.63}Fe_{0.03}O_2H$, Liu et al. 2019).

194

195   **XRD experiments**

196   The compression behavior of the δ-(Al,Fe)OOH samples were examined with a

197   membrane-type DAC (mDAC). This apparatus allowed the pressure in the sample

198   chamber to be increased without unloading it from the X-ray path, thus reducing time

199   interval between each measurement. Experimental pressure could be set precisely using

200   the gas control system. Flat 300 and 250 μm-culet diamonds were used as the anvils.

201   Rhenium plates pre-indented to thicknesses of 50 and 47 μm were used for the 300 and

202   250 μm-culet anvils, respectively, as gaskets. Crystals of δ-(Al,Fe)OOH were powdered

203   and then loaded into the sample hole in the gasket together with tungsten powder. One or

204   two ruby spheres were placed proximal to the sample. Compressed helium gas was

205   loaded into the sample chamber as the pressure medium at the National Institute for

206   Materials Science (NIMS), Japan (Takemura et al. 2001).

9

207   Two sets of compression experiments were performed, using δ-Fe12 (Run# DAF01)

208   and δ-Fe5 (Run# DAF02). In each run, XRD patterns were collected with the X-rays

209   focused on the tungsten powder before and after each XRD pattern of the sample was

210   collected. The pressure was determined using the equation of state (EoS) for tungsten

211   (Dorogokupets and Oganov 2006), and the ruby fluorescence method (Dewaele et al.

212   2008) was used to compare the pressure determined with the EoS for tungsten and to

213   ensure quasi-hydrostatic conditions in the sample chamber. To avoid the overlapping of

214   tungsten and δ-(Al,Fe)OOH peaks, tungsten patterns were collected without the δ-phase

215   before and after each XRD measurement on the samples. The average pressure drift was

216   0.3 GPa. The difference between the calculated pressures obtained using the EoS for

217   tungsten and the ruby fluorescence method was less than 0.9 GPa in each case. The

218   experimental pressures were increased up to 38 and 35 GPa in runs DAF01 and DAF02,

219   respectively, by tightening the four screws on the mDAC. The pressure was subsequently

220   increased to the maximum desired value by supplying helium gas to the unit. During the

221   decompression process, the gas was first released followed by loosening of the screws. In

222   the DAF02 experimental run, the ambient XRD pattern of δ-Fe5 was collected after

223   decompression. The ambient XRD patterns of the additional sample, the δ-

224    $(Al_{0.807(7)}{}^{57}Fe_{0.117(4)})OOH_{1.15(3)}$ (Fe/(Al+Fe) = 0.127(3), identical ratio to δ-Fe12 within

225   error), were also collected at the X-ray Crystallography Facility in the Beckman Institute

226   at the California Institute of Technology, where a Mo target (λ = 0.7107 Å) was employed.

227   The single crystal XRD analysis for the δ-$(Al_{0.807(7)}{}^{57}Fe_{0.117(4)})OOH_{1.15(3)}$ under

228   ambient conditions confirmed the structure of δ-AlOOH under ambient conditions (e.g.,

229   Suzuki et al. 2000) (space group as $P2_1nm$, the CIF file is in the deposit).

10

230   Angle dispersive powder XRD patterns were collected at the BL10XU beamline

231   (Ohishi et al. 2008). An imaging plate (Rigaku, R-AXIS IV^{++}) was used for acquiring the

232   XRD patterns, and the exposure time was 8 min. The X-ray wavelength was 0.4141(1) Å

233   (for compression and decompression in run# DAF01), 0.4152(2) Å (compression in run#

234   DAF02) and 0.4143(1) Å (decompression in run# DAF02). One dimensional diffraction

235   profiles were fitted with a pseudo-Voigt function using the PDIndexer software (Seto et

236   al. 2010). The 110, 101, 011, 111, 210, 211, 121, 220, 310, 002, 301, and 112 reflections

237   were employed to calculate the lattice parameters. The 101, 002, 211, 121, 220, 310, 301,

238   and 112 reflections were excluded from the calculations when they overlapped with

239   helium reflections. The 110, 211, and 220 reflections of tungsten were used for pressure

240   determination (Dorogokupets and Oganov 2006). The determination method of lattice

241   constants follows the previous study on Fe-free δ-AlOOH (Sano-Furukawa et al. 2009) to

242   compare the compressional behaviors of Fe-bearing and Fe-free δ-phases. Pressure vs.

243   unit cell volume (*P-V*) profiles obtained from the XRD experiments were fitted using a

244   spin crossover EoS with version 2.1.0 of the MINUTI software (Sturhahn 2018).

245

246   **Synchrotron Mössbauer spectroscopy experiments**

247   A wide-angled piston-cylinder DAC with 300 μm-culet/370 μm-beveled anvils was

248   used to generate high pressure conditions for the SMS experiments. A piece of δ-Fe13

249   with dimensions of 40 × 50 × 20 μm was cut from a larger crystallite in the same

250   synthesis run described above. A beryllium disk pre-indented to a thickness of 38 μm was

251   used as a gasket. The diameter of the sample hole in the gasket was 165 μm for 300 μm-

252   culet anvils. A mixture of 10–20 μm thick boron epoxy (amorphous boron powder:epoxy

11

253 = 4:1 by weight; Lin et al. 2003) was put on the side of a beryllium gasket hole. Two

254 ruby spheres were positioned beside the sample as pressure markers (Dewaele et al.

255 2008). Compressed neon gas was loaded into the sample chamber as a pressure medium

256 at the California Institute of Technology.

257 Time-domain SMS measurements were conducted on a single crystal of δ-Fe13 at

258 Sector 3-ID-B at the Advanced Photon Source (APS). The storage ring was operated in

259 top-up mode with 24 bunches separated by 153 ns. A high-resolution monochromator

260 was tuned to the 14.4125 keV nuclear transition energy of ^{57}Fe with a FWHM of about 1

261 meV (Toellner 2000). The beam was focused to an area of 10 by 14 μm^2 using a

262 Kirkpatrick-Baez mirror system. The time spectra were measured with an avalanche

263 photodiode detector positioned about 0.5 m downstream from the sample. A 10 μm thick

264 stainless steel (SS) foil with a natural abundance of ^{57}Fe was placed in the downstream

265 direction as a reference absorber for isomer shift measurements. At each compression

266 point, a spectrum was collected of the sample with and without the SS reference foil. The

267 isomer shift between the SS foil and α-iron metal was measured at the APS using a

268 radioactive source and found to be −0.100(3) mm/s with a corresponding FWHM (due to

269 the effect of site distribution) of 0.445(9) mm/s (Solomatova et al. 2017).

270 Synchrotron Mössbauer spectra were fitted with version 2.1.1 of the CONUSS

271 software (Sturhahn 2000, 2016), which implements a least-square algorithm to fit iron's

272 hyperfine parameters and material properties. The spectrum of the sample and sample

273 with SS were fitted simultaneously. For a single crystal, the orientation of the electric

274 field gradient tensor of each iron site must be specified with respect to the direction and

275 polarization of the X-ray using three Euler angles (α, β and γ). The orientation of the

12

276 crystal was determined through careful analysis of the reduced χ^2 and Monte Carlo

277 searches. The Euler angles of the high-spin site were calculated using the CONUSS

278 module, "kvzz" using the lattice parameters and atomic positions of δ-Fe13. The Euler

279 angles for the low-spin sites were determine through a Monte Carlo search and were

280 fixed with pressure.

281

282   **RESULTS**

283

284 **XRD experiments**

285   δ-Fe12   (δ-(Al$_{0.832(5)}$^{57}Fe$_{0.117(1)}$)OOH$_{1.15(3)}$,   Run#   DAF01)   and   δ-Fe5   (δ-

286 (Al$_{0.908(9)}$^{57}Fe$_{0.045(1)}$)OOH$_{1.14(3)}$, Run# DAF02) were compressed to 65 and 56 GPa,

287 respectively. The representative one-dimensional XRD patterns of the samples converted

288 from two-dimensional patterns are shown in Figure 1. The lattice constants (*a*, *b*, and *c*)

289 and unit cell volumes determined from the XRD data for δ-Fe12 and δ-Fe5 are

290 summarized in Tables 1 and 2, respectively. It should be noted that the tungsten pressure

291 scale does not include the errors of EoS parameters (V_0, K_0, K'), and therefore the

292 experimentally determined pressures in this study might be relatively smaller than the

293 other experimental studies (e.g., Duan et al. 2018). A potential pressure error might be up

294 to ~2%, as presumed in Sano-Furukawa et al. (2009).

295   Figure 2 shows the *P-V* profiles of the two samples during compression and

296 decompression. The unit cell volume obtained during decompression is plotted along

297 with the compressional profiles (Fig. 2). The *P-V* profiles of δ-Fe12 and δ-Fe5 show that

298 both δ-(Al,Fe)OOH phases undergo multiple structural transitions over the experimental

299 pressure ranges, related to the change of the hydrogen bonds (e.g., Sano-Furukawa et al.

13

300   2008, 2009, 2018; Kuribayashi et al. 2014) and spin transition in Fe^{3+} (Gleason et al.

301   2013; Otte et al. 2009). The associated characteristics are:

302   (1) asymmetric (ordered) hydrogen bonds + high-spin state (HOC-I-HS, space group

303    $P2_1nm$)

304   (2) symmetric hydrogen bonds + high-spin state (HS, $Pnnm$)

305   (2a) symmetric (disordered) hydrogen bonds + high-spin state (HOC-III-HS, $Pnnm$)

306   (2b) symmetric (proton-centered) hydrogen bonds + high-spin state (HC-HS, $Pnnm$)

307   (3) symmetric hydrogen bonds + low-spin state (LS, $Pnnm$).

308   It should be noted that the HOC-III-HS (2a) and HC-HS (2b) states cannot be

309   distinguished in the XRD data, as discussed in the previous studies regarding pure δ-

310   AlOOH. This is because the former structure (2a) has two crystallographically equivalent

311   hydrogen sites characterized by proton tunneling and further transition to (2b) does not

312   involve a detectable change in compressibility. For example, the recent ND experiment

313   on δ-AlOOH provided direct evidence that the order–disorder transition of the hydrogen

314   bond and the symmetrization occur at different pressure conditions (9.0 and 18.1 GPa,

315   respectively), and argued the importance of the hydrogen bond disorder as a precursor of

316   the symmetrization in understanding the physical properties of minerals under high

317   pressures (Sano-Furukawa et al. 2018). Therefore, the possible transition from HOC-III-

318   HS to HC-HS before the onset of HS–LS transition is not evaluated in this study.

319   The $P2_1nm$(HOC-I)-HS (1) and $Pnnm$(HOC-III)-HS (2a) states are separated by the

320   subtle kinks in the P-V profiles (Fig. 2) and the inversion of axial compressibility at ~10

321   GPa (Fig. 3). $Pnnm$-HS (2) and $Pnnm$-LS (3) are distinguished by a volume collapse at

322   ~32–40 GPa (Fig. 2). Profiles of normalized pressure (F) against Eulerian strain (f) also

14

323   demonstrate changes in compressibility that occur through the symmetrization of

324   hydrogen bonds and spin crossover (Fig. 4).

325   A second-order Birch-Murnaghan (BM) EoS was fitted to the P-V profiles of δ-Fe12

326   and δ-Fe5 with the $P2_1nm$ structure, while a third-order Birch-Murnaghan spin crossover

327   EoS (hereafter, spin crossover EoS) was fitted to the P-V profiles of δ-Fe12 and δ-Fe5

328   with the $Pnnm$ structure using the MINUTI software (Sturhahn 2018) (Fig. 5 and Table

329   3). We consider the elastic and spin state (i.e., $3d$ electrons of the Fe atoms) contributions

330   to the free energy of the sample. For the elastic contribution, we adopt an expression

331   corresponding to the commonly-used third-order Birch-Murnaghan EoS (3rd-order BM

332   EoS)

$$F_{\text{elastic}} = \frac{9}{2}V_{T0}K_{T0}f^2\{1+(K'_{T0}-4)f\}, \tag{1}$$

334   where the Eulerian strain is given by $f = \{(V_0/V)^{2/3}-1\}/2$, and V_0, K_{T0}, and K'_{T0} are the

335   unit cell volume, isothermal bulk modulus, and the pressure derivative of K_{T0} at room

336   temperature, respectively. The Eq. 1 with a fixed K'_{T0} of 4 is called as 2nd-order BM EoS.

337   For the spin contribution, we assume a set of spin states described by the number of

338   unpaired electron, volume-dependent energy, and orbital degeneracy. For a given

339   pressure P, the volume at room temperature is calculated by solving the spin crossover

340   EoS

$$P(V,300 \text{ K}) = P_{\text{elastic}}(V, 300 \text{ K}) + P_{\text{spin}}(V, 300 \text{K}). \tag{2}$$

342   For more details of the spin crossover EoS, we refer the reader to Chen et al. (2012) and

343   Sturhahn (2018).

344   A spin crossover EoS reproduces the behavior of δ-Fe12 and δ-Fe5 in the crossover

345   region (Fig. 5 and Table 3). The pressure condition where the unit cell volume changes

15

346   due to the HS–LS transition is 50% complete is determined for δ-Fe12 at 36.1 ± 0.7 GPa,

347   which is defined as the spin transition pressure. Although the volume collapse of δ-Fe5 is

348   very small due to the low Fe^{3+} content in the sample, it was nonetheless possible to

349   determine the spin transition pressure of 34.9 ± 1.1 GPa. The values of F were found to

350   decrease with increasing f through the spin crossover, which is seen clearly in both the

351   Fe-rich δ-Fe12 and the Fe-poor δ-Fe5 samples (Fig. 4). The isothermal bulk modulus (K_T)

352   and bulk sound velocity (v_Φ) of δ-Fe12 and δ-Fe5 also decrease in the spin crossover

353   (Fig. 6).

354

355   **SMS experiments**

356   Synchrotron Mössbauer spectra of δ-Fe13 were collected at 21.1(2), 31.8(8), 45(2),

357   59(2), 67.5(5), and 78.6(5) GPa (Fig. 7). The results of SMS experiments demonstrate

358   that the HS–LS transition in δ-Fe13 is completed by 45 GPa (Fig. 8), which is similar to

359   the pressure conditions at which volume collapse is completed in the P-V profiles of δ-

360   Fe12 and δ-Fe5. At 21.1 and 31.8 GPa, one high-spin Fe^{3+}-like site was required to fit the

361   spectra with a quadrupole splitting value of ~0.4 mm/s and isomer shift of 0.2 mm/s, thus

362   we find that 100% of the iron in this phase is Fe^{3+} (see Figs. 7 and 8, and Table 4, which

363   include reported uncertainties).

364   We attempted to fit the spectra above 32 GPa with one low-spin site, but the best

365   model with one low-spin site resulted in a reduced χ^2 of 5. Although δ-Fe13 is

366   characterized by one crystallographic Fe site, the Mössbauer spectra above 32 GPa

367   require two distinct nuclear sites. It is possible that the crystal quality decreased and/or

368   next nearest neighbor interactions explain the additional Mössbauer-site. At pressures of

16

369   45 GPa and higher, the two low-spin Fe^{3+}-like sites are characterized as follows: one with

370   a quadrupole splitting value of ~1.14–1.32 mm/s and a second site with a quadrupole

371   splitting value of 1.73–2.01 mm/s with weight fractions of 67% and 33%, respectively

372   (Figs. 7 and 8, and Table 4). The isomer shifts with values 0.107–0.249 mm/s follow a

373   negative trend with pressure indicating an increase of the s-electron density at the iron

374   sites that is probably caused by volume decrease.

375   For all evaluations of the time spectra, we assumed axial symmetry of the electric field

376   gradient tensor at the iron sites. Therefore, only two Euler angles, α and β, need to be

377   considered. For the HS site, these Euler angles were calculated from the lattice

378   parameters and atomic positions of this phase (Table 5). For the LS sites α and β were

379   determined from a Monte Carlo search resulting in values of 296° and 261° for one of the

380   LS sites and 22° and 253° for the other site, respectively.

381

382   **DISCUSSION**

383   Subtle kinks in the *P-V* profiles for δ-Fe12 and δ-Fe5 are observed at approximately 10

384   GPa (Fig. 2), which may be a result of a structural transition from ordered ($P2_1nm$(HOC-

385   I)-HS) to disordered hydrogen bonds (*Pnnm*(HOC-III)-HS), as observed in XRD and ND

386   measurements on pure δ-AlOOH (Sano-Furukawa et al. 2009, 2018; Kuribayashi et al.

387   2014). The *a*/*c* and *b*/*c* values decrease rapidly with increasing pressure below ~10 GPa,

388   whereas the *a*/*b* values increase up to ~10 GPa. The trend in the axial compressibility is

389   reversed above 10 GPa such that the *a* and *b* axes are less compressible than the *c* axis

390   (Fig. 3). Our finding that the *a* and *b* axes are less compressible than the *c*-axis above 10

391   GPa are corroborated by computational studies for pure δ-AlOOH showing that the

17

392   hydrogen bonds in the *Pnnm* structure are stronger than those in the *P2₁nm* phase

393   (Cortona 2017; Tsuchiya and Tsuchiya 2009; Tsuchiya et al. 2002; Kang et al. 2017;

394   Pillai et al. 2018). Such an inversion of the compressibility is also observed in δ-AlOOH

395   at 8–10 GPa (Sano-Furukawa et al. 2009, 2018; Kuribayashi et al. 2014). The hydrogen

396   bonds in the *Pnnm* structures are almost parallel to the ⟨120⟩ direction, so the effects of

397   these hydrogen bonds on structures and physical properties are stronger along the *b* axis

398   than the *a* axis (Kuribayashi et al. 2014), while the compressibility of the *c* axis is

399   unlikely to be modified. The pressure conditions of inversions of compressibility in δ-

400   Fe12 and δ-Fe5 are very close to that of pure δ-AlOOH (Sano-Furukawa et al. 2009,

401   2018; Kuribayashi et al. 2014). Our data demonstrates that Fe incorporation into the δ-

402   phase is insensitive to the pressure condition of *P2₁nm* (ordered-hydrogen bond)–*Pnnm*

403   (disordered hydrogen bond) transition.

404   The SMS experiments show that octahedrally-coordinated Fe^{3+} in δ-Fe13 undergoes a

405   HS–LS transition at the pressure range of 32–45 GPa. Collapse in unit cell volume is also

406   observed in the δ-Fe12 and δ-Fe5 samples within this pressure range, likely as a result of

407   the Fe^{3+} spin transition. The spin-crossover pressures estimated from the *P-V* profiles of

408   δ-Fe12 and δ-Fe5 are within the pressure range of ~32–40 GPa, which is ~10 GPa lower

409   than that of ε-FeOOH examined with XRD experiments (46–54 GPa, Gleason et al.

410   2013), suggesting that the LS state would be stabilized at lower pressures with decreasing

411   FeOOH concentration in the solid solution. The positive correlation between Fe content

412   and spin-transition pressure has also been reported for the MgO (periclase)–FeO (wüstite)

413   solid solution. The spin-transition pressure of Fe^{2+} in (Mg,Fe)O is reduced with

414   decreasing FeO content (e.g., Lin et al. 2005; Fei et al. 2007; Solomatova et al. 2016).

18

415 Our results demonstrate that this relationship also applies to the δ-AlOOH–ε-FeOOH

416 solid solution.

417 The spin transition in Fe^{3+} is also observed in the new hexagonal aluminous phase

418 (NAL phase). NAL phase has the chemical formula of $AB_2C_6O_{12}$ (A = Na^+, K^+, Ca^{2+}; B =

419 Mg^{2+}, Fe^{2+}, Fe^{3+}; C = Al^{3+}, Si^{4+}, Fe^{3+}) with the space group of $P6_3/m$ (Gasparik et al.

420 2000; Miura et al. 2000; Miyajima et al. 2001), and is considered to exist in a basaltic

421 layer of the slab subducted to the upper region of the lower mantle (e.g., Irifune and

422 Ringwood 1993). The recent experimental study under room temperature reported that

423 the Fe-bearing ($Na_{0.71}Mg_{2.05}$ $Fe^{2+}_{0.09}Al_{4.62}Fe^{3+}_{0.17}Si_{1.16}O_{12}$) NAL phase showed 1.0%

424 volume reduction at 33–47GPa associated with the Fe spin transition (Wu et al. 2016). In

425 the NAL phase, only Fe^{3+} in the octahedral C site undergoes the spin transition at the

426 pressure conditions of the upper region of lower mantle, while Fe^{2+} and Fe^{3+} in the

427 trigonal-prismatic B site maintain high-spin states up to at least 80 GPa (Wu et al. 2016;

428 Hsu 2017). Therefore, only Fe^{3+} in the octahedral site contributes to the spin transition in

429 NAL phase at that pressure range, which could explain why the width of the spin

430 crossover where the softening occurs is slightly narrower in δ-(Al,Fe)OOH samples (Fig.

431 9).

432 It should be noted that a HOC-III–HC transition without an observable change in the

433 P-V compression trend may occur in the δ-(Al,Fe)OOH samples before or concurrently

434 with the spin crossover, because the HOC-III–HC transition pressure of δ-AlOOH is ~20

435 GPa (Sano-Furukawa et al. 2018) and for ε-FeOOH it ranges from ~10 to ~43 GPa

436 (Thompson et al. 2017; Gleason et al. 2013), respectively. Further studies are required to

19

437   investigate the relationship between hydrogen symmetrization and spin state in the δ-

438   AlOOH–ε-FeOOH solid solution.

439

440   **IMPLICATIONS**

441   In hydrous rock systems, δ-AlOOH may form a solid solution with isostructural

442    $MgSiO_4H_2$ Phase H (Suzuki et al. 2000; Ohtani et al. 2001; Nishi et al. 2014, 2015; Ohira

443   et al. 2014; Walter et al. 2015; Panero and Caracas 2017; Liu et al. 2019) and ε-FeOOH

444   components (Nishi et al. 2015, 2017; Kawazoe et al. 2017; Liu et al. 2019). Therefore,

445   the incorporation of MgSi- and Fe-endmember components into the δ-phase would need

446   to be considered in interpretations of lower mantle seismic observations. However, Nishi

447   et al. (2018) found that the incorporation of a Phase H component into the δ-phase has

448   little effect on the density of the δ-phase because the differences of volume and mole

449   weight between δ-AlOOH and $MgSiO_4H_2$ Phase H are only 1.0–1.2% and 1.3% at the

450   pressure condition from top- to mid-lower mantle. Therefore, the physical properties of

451   binary δ-AlOOH–ε-FeOOH solid solution, investigated in this study, are important to

452   understand the behavior of ternary δ-AlOOH–ε-FeOOH–phase H solid solution under

453   lower mantle conditions.

454   Figure 9 shows the isothermal bulk modulus, density, bulk sound velocity, and the

455   ratio of density to bulk sound velocity for δ-Fe12, δ-Fe5, several hydrous phases, and Fe-

456   bearing NAL phase at pressures between the top- and mid-lower mantle. Our results

457   show that the isothermal bulk modulus of low-spin δ-Fe12 is larger than those of δ-

458   AlOOH, $MgSiO_4H_2$ Phase H, and ε-FeOOH, and that of low-spin δ-Fe5 is comparable to

459   that reported for δ-AlOOH and ε-FeOOH, except for the pressure conditions of the spin

20

460 crossover (Fig. 9a). DFT calculations suggest that the bulk modulus of low-spin ε-

461 FeOOH is 4–8 % higher than the bulk modulus of δ-AlOOH at pressures of the entire

462 lower mantle and 0 K (Thompson et al. 2017). Interestingly, although the bulk modulus

463 trends of δ-Fe12 and δ-Fe5 overlap within error (see Fig. 6), the values for the Fe-rich δ-

464 Fe12 sample are systematically 2–3 % higher than those of the Fe-poor δ-Fe5 sample

465 above 45 GPa in spite of an only ~7 at% difference in Fe content. Therefore, our results

466 suggest that the bulk modulus of low spin δ-(Al,Fe)OOH may be sensitive to smaller

467 amounts of Fe incorporation than the computational study predicted (Thompson et al.

468 2017). This sensitive relationship between the bulk modulus and Fe content δ-

469 (Al,Fe)OOH may influence in understanding the origin of seismic anomalies in the lower

470 mantle. The ρ, v_Φ, and their ratio (ρ/v_Φ) of pure δ-AlOOH were calculated along a mantle

471 geotherm (Brown and Shankland, 1981) to be 11–12% lower, 5–8% higher, and 16–18%

472 lower than those of PREM, respectively, implying that the low ρ/v_Φ ratio of pure δ-

473 AlOOH can help identify its potential presence in the lower mantle (Duan et al. 2018).

474 The incorporation of Fe into δ-(Al,Fe)OOH decreases the gaps of these properties

475 between δ-phase and PREM, due to the relatively large mass of Fe. Nevertheless, δ-Fe12

476 and δ-Fe5 samples still exhibit higher v_Φ and lower ρ and ρ/v_Φ ratio, compared to PREM.

477 Therefore, a low ρ/v_Φ anomaly caused by the presence of an iron-bearing δ-phase likely

478 occurs in the lower mantle, with the exception of the spin crossover region.

479   If subducting materials including the hydrous solid solution are transported to the

480 lower mantle, this hydrous phase might accumulate in deep lower mantle regions over

481 geologic time. Continuous transport of subducted slab material to the deep lower mantle

482 has been supported by geophysical simulations and geochemical studies (e.g., Tackley

21

483   2011; Bower et al. 2011; van der Meer et al. 2010). One of the possible contributions of

484   the hydrous δ-AlOOH–ε-FeOOH–phase H solid solution is a high-v_Φ anomaly in the

485   lower mantle. For example, the approximately 0.3% v_Φ increase is observed at the

486   boundary regions of large low shear velocity provinces (Masters et al. 2000). Those

487   provinces are located at a depth of ~2,000–2,890 km beneath the Pacific Ocean and the

488   Atlantic Ocean–the western and southern part of the African continent, and are adjacent

489   to the path of a subducting slab. If we apply the thermal parameters of δ-AlOOH reported

490   by Duan et al. (2018) to δ-Fe5 or δ-Fe12, this anomaly can be explained by the

491   accumulation of ~6–8 wt% δ-Fe5 or δ-Fe12, which is ~9% lower than the proportion of

492   hydrous δ-AlOOH–ε-FeOOH–phase H solid solution (δ-$(Mg_{0.11}Fe_{0.03}Si_{0.2}Al_{0.63})$OOH,

493   termed as "Al-rich Phase H" in Liu et al. 2019) formed in the oceanic basalt + 3.5 wt.%

494   H_2O system (Liu et al. 2019). The accumulation of ~6–8 wt% δ-Fe5 or δ-Fe12 is

495   equivalent to the presence of only ~1 wt% H_2O.

496   The low ρ/v_Φ character of δ-(Al,Fe)OOH becomes inverted to a high ρ/v_Φ within the

497   spin crossover due to the softening of the bulk modulus (Figs. 6 and 9). Although the spin

498   transition of Fe^{3+} in the octahedral site is also observed in the Fe-bearing NAL phase, the

499   transition pressure is lower and the width of spin crossover is slightly narrower in the δ-

500   (Al,Fe)OOH samples than the Fe-bearing NAL phase (Wu et al. 2016). The spin

501   crossover and resultant softening are influenced by temperature and valance of Fe. For

502   example, the onset pressure for the LS state in $(Mg_{0.75}Fe_{0.25})$O ferropericlase increases

503   from ~50 GPa at 300 K to 65 GPa at 1200 K, with an appreciable increase in the width of

504   the spin crossover region (e.g., Mao et al. 2011). On the other hand, a computational

505   study by Hsu (2017) showed that the spin transition pressure of Fe^{3+} in the octahedral site

22

506   of the NAL phase (~40 GPa) remains mostly invariant to temperature and the width

507   moderately increases with temperature. This would imply that for δ-(Al,Fe)OOH at 1200

508   K, the estimated temperature of a subducted slab at the top of the lower mantle (Ricard et

509   al. 2005; Kirby et al. 1996), the spin transition pressure will likely be unchanged from

510   that measured at 300 K and the softening of bulk modulus remains appreciable. The spin

511   transition pressure and the width of spin crossover are slightly lower and narrower in the

512   δ-(Al,Fe)OOH samples than the Fe-bearing NAL phase (Fig. 9). Therefore, the high ρ/v_Φ

513   of δ-(Al,Fe)OOH in the spin crossover region would be observable at the pressure

514   conditions of the uppermost lower mantle, especially under relatively cooler

515   temperatures, such as those calculated for a subducted slab. Seismological studies have

516   reported the laterally heterogeneous ρ and v_Φ in the upper region of the lower mantle

517   (Masters et al. 2000; Trampert et al. 2004), and the presence of δ-(Al,Fe)OOH may

518   explain these anomalies.

519   In this section, we have focused on drawing comparisons of our results for the δ-

520   (Al,Fe)OOH solid solution across the spin transition, with those of endmember phases (δ-

521   AlOOH, ε-FeOOH, and $MgSiO_4H_2$ Phase H), the Fe-bearing NAL phase, and PREM. We

522   have also suggested that δ-(Al,Fe)OOH could cause low ρ/v_Φ anomaly in the lower

523   mantle, except for the conditions where the spin crossover occurs. Specifically, δ-

524   (Al,Fe)OOH has high ρ/v_Φ ratio due to the spin crossover, which occurs under uppermost

525   lower mantle conditions. These anomalies in geophysical properties of δ-(Al,Fe)OOH

526   suggest that the presence of δ-(Al,Fe)OOH could be detectable and provide new insight

527   for understanding the heterogeneity in the lower mantle.

528

529   **ACKNOWLEDGMENTS**
530
552

553

554   **REFERENCES CITED**
555
556   Abe, R., Shibazaki, Y., Ozawa, S., Ohira, I., Tobe, H., and Suzuki, A. (2018) In situ X-

557   ray diffraction studies of hydrous aluminosilicate at high pressure and

558   temperature. Journal of Mineralogical and Petrological Sciences, 113, 106–111.

559   Bell, D.R., and Rossman, G.R. (1992) Water in Earth's mantle: the role of nominally

560   anhydrous minerals. Science, 255, 1391–1397.

561   Bindi, L., Nishi, M., Tsuchiya, J., and Irifune, T. (2014) Crystal chemistry of dense

562   hydrous magnesium silicates: The structure of Phase H, $MgSiH_2O_4$ synthesized at

563   45 GPa and 1000 °C. American Mineralogist, 99, 1802–1805.

564   Bower, D.J., Gurnis, M., and Seton, M. (2011) Lower mantle structure from

565   paleogeographically constrained dynamic Earth models. Geochemistry

566   Geophysics Geosystems, 14, 44–63.

567   Bronstein, Y., Depondt, P., and Finocchi F. (2017) Thermal and nuclear quantum effects

568   in the hydrogen bond dynamical symmetrization phase transition of δ-AlOOH.

569   European Journal of Mineralogy, 29, 385–395.

570   Brown, J.M., and Shankland, T.J. (1981) Thermodynamic parameters in the Earth as

571   determined from seismic profiles. Geophysical Journal of the Royal Astronomical

572   Society, 66, 579–596.

573   Cedillo, A., Torrent, M., and Cortona, P. (2016) Stability of the different AlOOH phases

574   under pressure. Journal of Physics: Condensed Matter, 28, 185401.

575   Chen, B., Jackson, J.M., Sturhahn, W., Zhang, D., Zhao, J., Wicks, J.K., and Murphy,

576   C.A. (2012) Spin crossover equation of state and sound velocities of

25

577   (Mg$_{0.65}$Fe$_{0.35}$)O ferropericlase to 140 GPa. Journal of Geophysical Research, 117,

578   B08208.

579 Cortona, P. (2017) Hydrogen bond symmetrization and elastic constants under pressure

580   of δ-AlOOH. Journal of Physics: Condensed Matter, 29, 325505.

581 Dewaele A., Torrent, M., Loubeyre, P., and Mezouar, M. (2008) Compression curves of

582   transition metals in the Mbar range: Experiments and projector augmented-wave

583   calculations. Physical Review B, 78, 104102.

584 Dorogokupets, P.I., and Oganov, A.R. (2006) Equations of state of Al, Au, Cu, Pt, Ta,

585   and W and revised ruby pressure scale. Doklady Earth Sciences, 410, 1091–1095.

586 Duan, Y., Sun, N., Wang, S., Li, X., Guo, X., Ni, H., Prakapenka, V.B., and Mao, Z.

587   (2018) Phase stability and thermal equation of state of δ-AlOOH: Implication for

588   water transportation to the Deep Lower Mantle. Earth and Planetary Science

589   Letters, 494, 92–98.

590 Dziewonski, A.M., and Anderson, D. L. (1981) Preliminary reference Earth model.

591   Physics of the Earth and Planetary Interiors, 25, 297–356.

592 Fei, Y., Zhang, L., Corgne, A., Watson, H., Ricolleau, A., Meng, Y., and Prakapenka, V.

593   (2007) Spin transition and equations of state of (Mg, Fe)O solid solutions.

594   Geophysical Research Letters, 34, L17307.

595 Fukuyama, K., Ohtani, E., Shibazaki, Y., Kagi, H., and Suzuki, A. (2017) Stability field

596   of phase Egg, AlSiO$_3$OH at high pressure and high temperature: possible water

597   reservoir in mantle transition zone. Journal of Mineralogical and Petrological

598   Sciences, 112, 31–35.

599   Gasparik, T., Tripathi, A., and J.B. Parise. (2000) Structure of a new Al-rich phase, [K,

600   Na]$_{0.9}$[Mg, Fe]$_2$[Mg, Fe, Al, Si]$_6$O$_{12}$, synthesized at 24 GPa. American

601   Mineralogist, 85, 613–618.

602   Gleason, A.E., Quiroga, C.E., Suzuki, A., Pentcheva, R., and Mao, W.L. (2013)

603   Symmetrization driven spin transition in ε-FeOOH at high pressure. Earth and

604   Planetary Science Letters, 379, 49–55.

605   Hsu, H. (2017) First-principles study of iron spin crossover in the new hexagonal

606   aluminous phase. Physical Review B, 95, 020406.

607   Irifune, T. and Ringwood, A.E. (1993) Phase transformations in subducted oceanic crust

608   and buoyancy relationships at depths of 600–800 km in the mantle. Earth and

609   Planetary Science Letters, 117, 101–110.

610   Kagi, H., Ushijima, D., Sano-Furukawa, A., Komatsu, K., Iizuka, R., Nagai, T., and

611   Nakano, S. (2010) Infrared absorption spectra of δ-AlOOH and its deuteride at

612   high pressure and implication to pressure response of the hydrogen bonds. Journal

613   of Physics: Conference Series, 215, 012052.

614   Kaminsky, F.V. (2017) The Earth's Lower Mantle, Composition and Structure, 331 p.

615   Springer International Publishing AG, Switzerland.

616   Kang, D., Feng, Y.-X., Yuan, Y., Ye, Q.-J., Zhu, F., Huo, H.-Y., Li, X.-Z., and Wu, X.

617   (2017) Hydrogen-bond symmetrization of δ-AlOOH. Chinese Physics Letters, 34,

618   108301.

619   Kawazoe, T., Ohira, I., Ishii, T., Boffa Ballaran, T., McCammon, C., Suzuki, A., and

620   Ohtani, E. (2017), Single crystal synthesis of δ-(Al,Fe)OOH. American

621   Mineralogist, 102, 1953–1956.

27

622   Kirby, S.H., Stein, S., Okal, E.A., and Rubie, D.C. (1996) Metastable mantle phase

623   transformations and deep earthquakes in subducting oceanic lithosphere. Reviews

624   of Geophysics, 34, 261–306.

625   Komatsu, K., Kuribayashi, T., Sano, A., Ohtani, E., and Kudoh, Y. (2006)

626   Redetermination of the high-pressure modification of AlOOH from single-crystal

627   synchrotron data. Acta Crystallographica Section E, 62, i216–218.

628   Kuribayashi, T., Sano-Furukawa, A., and Nagase, T. (2014) Observation of pressure-

629   induced phase transition of δ-AlOOH by using single‑crystal synchrotron X-ray

630   diffraction method. Physics and Chemistry of Minerals, 41, 303–312.

631   Li, S., Ahuja, R., and Johansson, B. (2006) The elastic and optical properties of the high-

632   pressure hydrous phase δ-AlOOH. Solid State Communications, 137, 101–106.

633   Lin, J.F., Shu, J., Mao, H.K., Hemley, R.J., and Shen, G. (2003) Amorphous boron gasket

634   in diamond anvil cell research. Review of Scientific Instruments, 74, 4732–4736.

635   Lin, J.F., Struzhkin, V.V., Jacobsen, S.D., Hu, M.Y., Chow, P., Kung, J., Liu, H., Mao,

636   H.-k., and Hemley, R. J. (2005) Spin transition of iron in magnesiowüstite in the

637   Earth's lower mantle. Nature, 436, 377–380.

638   Liu, X., Matsukage, K.N., Nishihara, Y., Suzuki, T., and Takahashi, E. (2019) Stability of

639   the hydrous phases of Al-rich Phase D and Al-rich Phase H in deep subducted

640   oceanic crust. American Mineralogist, 104, 64–72.

641   Mao, Z., Lin, J.-F., Liu, J., and Prakapenka, V.B. (2011) Thermal equation of state of

642   lower-mantle ferropericlase across the spin crossover. Geophysical Research

643   Letters, 38, L23308.

644   Mashino, I., Murakami, M., and Ohtani, E. (2016) Sound velocities of δ-AlOOH up to

645   core-mantle boundary pressures with implications for the seismic anomalies in the

646   deep mantle. Journal of Geophysical Research: Solid Earth, 121, 595–609.

647   Masters, G., Laske, G., Bolton, H., and Dziewonski, A. (2000) The relative behavior of

648   shear velocity, bulk sound speed, and compressional velocity in the mantle:

649   Implications for chemical and thermal structure. In S.-I. Karato, A. Forte, R.

650   Liebermann, G. Masters, and L. Stixrude, Eds., Earth's deep interior: Mineral

651   physics and tomography from the atomic to the global scale, Geophysical

652   Monograph 117, p. 63–87. the American Geophysical Union, U.S.A

653   Miura, H., Hamada, Y., Suzuki, T., Akaogi, M., Miyajima, N., and Fujino, K. (2000)

654   Crystal structure of $CaMg_2Al_6O_{12}$, a new Al-rich high pressure form. American

655   Mineralogist, 85, 1799–1803.

656   Miyajima, N., Yagi, T., Hirose, K., Kondo, T., Fujino, K., and Miura, H. (2001) Potential

657   host phase of aluminum and potassium in the Earth's lower mantle. American

658   Mineralogist, 86, 740–746.

659   Nishi, M., Irifune, T., Tsuchiya, J., Tange, Y., Nishihara, Y., Fujino, K., Higo, Y. (2014)

660   Stability of hydrous silicate at high pressures and water transport to the deep

661   lower mantle. Nature Geoscience, 7, 224–227.

662   Nishi, M., Irifune, T., Gréaux, S., Tange, Y., Higo, Y. (2015) Phase transitions of

663   serpentine in the lower mantle. Physics of the Earth and Planetary Interiors, 245,

664   52–58.

665   Nishi, M., Kuwayama, Y., Tsuchiya, J., and Tsuchiya, T. (2017) The pyrite-type high-

666   pressure form of FeOOH. Nature, 547, 205–208.

29

667   Nishi, M., Tsuchiya, J., Arimoto, T., Kakizawa, S., Kunimoto, T., Tange, Y., Higo, Y.,

668   Irifune, T. (2018) Thermal equation of state of $MgSiO_4H_2$ phase H determined by

669   in situ X-ray diffraction and a multianvil apparatus. Physics and Chemistry of

670   Minerals, 45, 995–1001.

671   Nishihara, Y., and Matsukage, K.N. (2016) Iron-titanium oxyhydroxides as water carriers

672   in the Earth's deep mantle. American Mineralogist, 101, 919–927.

673   Ohira, I., Ohtani, E., Sakai, T., Miyahara, M., Ohishi, Y., Hirao, N., and Nishijima, M.

674   (2014) Stability of a hydrous δ-phase, $AlOOH-MgSiO_2(OH)_2$, and a mechanism

675   for water transport into the base of lower mantle. Earth and Planetary Science

676   Letters, 401, 12–17.

677   Ohishi, Y., Hirao, N., Sata, N., Hirose, K., and Takata, M. (2008) Highly intense

678   monochromatic X-ray diffraction facility for high-pressure research at SPring-8.

679   High Pressure Research, 28, 163–173.

680   Ohtani, E. (2005) Water in the mantle. Elements, 1, 25–30.

681   Ohtani, E. (2015) Hydrous minerals and the storage of water in the deep mantle.

682   Chemical Geology, 418, 6–15.

683   Ohtani, E., Amaike, Y., Kamada, S., Ohira, I., and Mashino, I. (2016) Stability of

684   hydrous minerals and water reservoirs in the deep Earth interior. In H. Terasaki,

685   and R. A. Fischer, Eds., Deep Earth: Physics and chemistry of the lower mantle

686   and core, Geophysical Monograph 217, p. 265–275. the American Geophysical

687   Union, U.S.A.

30

688   Ohtani, E., Litasov, K., Suzuki, A., and Kondo, T. (2001) Stability field of new hydrous

689   phase, δ-AlOOH, with implications for water transport into the deep mantle.

690   Geophysical Research Letters, 28, 3991–3994.

691   Okamoto, K., and Maruyama, S. (2004) The Eclogite–Garnetite transformation in the

692   MORB + H_2O system. Physics of the Earth and Planetary Interiors, 146, 283–296.

693   Otte, K., Pentcheva, R., Schmahl, W.W., and Rustad, J.R. (2009) Pressure-induced

694   structural and electronic transitions in FeOOH from first principles. Physical

695   Review B, 80, 205116.

696   Pamato, M.G., Myhill, R., Boffa Ballaran, T., Frost, D.J., Heidelbach, F., and Miyajima,

697   N. (2015) Lower-mantle water reservoir implied by the extreme stability of a

698   hydrous aluminosilicate. Nature Geoscience, 8, 75–79.

699   Panero, W.R., and Caracas, R. (2017) Stability of phase H in the $MgSiO_4H_2$–AlOOH–

700   SiO_2 system. Earth and Planetary Science Letters, 463, 171–177.

701   Panero, W.R., and Stixrude, L.P. (2004) Hydrogen incorporation in stishovite at high

702   pressure and symmetric hydrogen bonding in δ-AlOOH. Earth and Planetary

703   Science Letters, 221, 421–431.

704   Pearson, D.G., Brenker, F.E., Nestola, F., McNeill, J., Nasdala, L., Hutchison, M.T.,

705   Matveev, S., Mather, K., Silversmit, G., Schmitz, S., Vekemans, B., and Vincze,

706   L. (2014) Hydrous mantle transition zone indicated by ringwoodite included

707   within diamond. Nature, 507, 221–224.

708   Pernet, M., Joubert, J.C., and Berthet-Colominas, C. (1975) Etude par diffraction

709   neutronique de la forme haute pression de FeOOH. Solid State Communications,

710   17, 1505–1510.

31

711   Pillai, S.B., Jha, P.K., Padmalal, A., Maurya, D.M., and Chamyal, L.S. (2018) First

712   principles study of hydrogen bond symmetrization in δ-AlOOH. Journal of

713   Applied Physics, 123, 115901.

714   Ricard, Y., Mattern, E., and Matas, J. (2005) Synthetic tomographic images of slabs from

715   mineral physics. In R. D. Van Der Hilst, J. D. Bass, J. Matas, and J. Trampert,

716   Eds., Earth's Deep Mantle: Structure, Composition, and Evolution, Geophysical

717   Monograph 160, p. 283–300. the American Geophysical Union, U.S.A

718   Sano, A., Ohtani, E., Kubo, T., and Funakoshi, K-i. (2004) In situ X-ray observation of

719   decomposition of hydrous aluminumsilicate AlSiO₃OH and aluminum oxide

720   hydroxide d-AlOOH at high pressure and temperature. Journal of Physics and

721   Chemistry of Solids, 65, 1547–1554.

722   Sano, A., Ohtani, E., Kondo, T., Hirao, N., Sakai, T., Sata, N., Ohishi, Y., and Kikegawa

723   T. (2008) Aluminous hydrous mineral δ-AlOOH as a carrier of hydrogen into the

724   core-mantle boundary. Geophysical Research Letters, 35, L03303.

725   Sano-Furukawa, A., Komatsu, K., Vanpeteghem, C.B., and Ohtani, E. (2008) Neutron

726   diffraction study of δ-AlOOD at high pressure and its implication for

727   symmetrization of the hydrogen bond. American Mineralogist, 93, 1558–1567.

728   Sano-Furukawa, A., Kagi, H., Nagai, T., Nakano, S., Fukura, S., Ushijima, D., Iizuka, R.,

729   Ohtani, E., and Yagi, T. (2009) Change in compressibility of δ-AlOOH and δ-

730   AlOOD at high pressure: A study of isotope effect and hydrogen-bond

731   symmetrization. American Mineralogist, 94, 1255–1261.

732   Sano-Furukawa, A., Hattori, T., Komatsu, K., Kagi, H., Nagai, T., Molaison, J.J., dos

733   Santos, A.M., and Tulk, C.A. (2018) Direct observation of symmetrization of

32

734   hydrogen bond in δ-AlOOH under mantle conditions using neutron diffraction.

735   Scientific Reports, 8, 15520.

736   Seto, Y., Nishio-Hamane, D., Nagai, T., and Sata, N. (2010) Development of a software

737   suite on X-ray diffraction experiments. The Review of High Pressure Science and

738   Technology, 20, 269–276 (in Japanese).

739   Smyth, J.R., and Jacobsen, S.D. (2006) Nominally anhydrous minerals and Earth's deep

740   water cycle. In S.D. Jacobsen, and S. van der Lee Eds., Earth's Deep Water Cycle,

741   Geophysical Monograph Series 168, p. 1–11. the American Geophysical Union,

742   U.S.A

743   Solomatova, N.V., Jackson, J.M., Sturhahn, W., Wicks, J.K., Zhao, J., Toellner, T.S.,

744   Kalkan, B., and Steinhardt, W.M. (2016) Equation of state and spin crossover of

745   (Mg,Fe)O at high pressure, with implications for explaining topographic relief at

746   the core-mantle boundary. American Mineralogist, 101, 1084–1093.

747   Solomatova, N.V., Jackson, J.M., Sturhahn, W., Rossman, G.R., and Roskosz, M. (2017)

748   Electronic environments of ferrous iron in rhyolitic and basaltic glasses at high

749   pressure. Journal of Geophysical Research: Solid Earth, 122, 6306–6322.

750   Sturhahn, W. (2000) CONUSS and PHOENIX: Evaluation of nuclear resonant scattering

751   data. Hyperfine Interactions, 125, 149–172.

752   ——— (2016) CONUSS (COherent NUclear resonant Scattering by Single crystals).

753   Open source software, http://www.nrixs.com.

754   ——— (2018) MINUTI (MINeral physics UTIlities). Open source software,

755   http://www.nrixs.com.

33

756   Suzuki, A. (2009) Compressibility of the high-pressure polymorph of AlOOH to 17 GPa.

757   Mineralogical Magazine, 73, 479–485.

758   ——— (2010) High-pressure X-ray diffraction study of ε-FeOOH. Physics and

759   Chemistry of Minerals, 37, 153–157

760   ——— (2016) Pressure–volume–temperature equation of state of ε-FeOOH to 11 GPa

761   and 700 K. Journal of Mineralogical and petrological Science, 111, 420–424.

762   Suzuki, A., Ohtani, E., and Kamada, T. (2000) A new hydrous phase δ-AlOOH

763   synthesized at 21 GPa and 1000 °C. Physics and Chemistry of Minerals, 27, 689–

764   693.

765   Tackley, P.J. (2011) Living dead slabs in 3-D: The dynamics of compositionally-

766   stratified slabs entering a ''slab graveyard'' above the core-mantle boundary.

767   Physics of the Earth and Planetary Interiors, 188, 150–162.

768   Takemura, K., Sahu, P.Ch., Kunii, Y., and Toma, Y. (2001) Versatile gas-loading system

769   for diamond-anvil cells. Review of Scientific Instruments, 72, 3873–3876.

770   Thompson E.C., Campbell, A. J., and Tsuchiya, J. (2017) Elasticity of ε-FeOOH: Seismic

771   implications for Earth's lower mantle. Journal of Geophysical Research: Soild

772   Earth, 122, 5038–5047.

773   Toellner, T.S. (2000) Monochromatization of synchrotron radiation for nuclear resonant

774   scattering experiments. Hyperfine Interactions, 125, 3–28.

775   Trampert, J., Deschamps, F., Resovsky, J., and Yuen, D. (2004) Probabilistic tomography

776   maps chemical heterogeneities throughout the lower mantle. Science, 306, 853–

777   856.

778   Tschauner, O., Huang, S., Greenberg, E., Prakapenka, V.B., Ma, C., Rossman, G.R.,

779   Shen, A.H., Zhang, D., Newville, M., Lanzirotti, A., and Tait, K. (2018) Ice-VII

780   inclusions in diamonds: Evidence for aqueous fluid in Earth's deep mantle.

781   Science, 359, 1136–1139.

782   Tsuchiya, J. and Mookherjee, M. (2015) Crystal structure, equation of state, and

783   elasticity of phase H ($MgSiO_4H_2$) at Earth's lower mantle pressures. Scientific

784   Reports, 5, 15534.

785   Tsuchiya, J. and Tsuchiya, T. (2009) Elastic properties of δ-AlOOH under pressure: First

786   principles investigation. Physics of the Earth and Planetary Interiors, 174, 122–

787   127.

788   Tsuchiya, J., Tsuchiya, T., Tsuneyuki, S., and Yamanaka T. (2002), First principles

789   calculation of a high-pressure hydrous phase, δ-AlOOH. Geophysical Research

790   Letters, 29, 1909.

791   van der Meer, D.G., Spakman, W., van Hinsbergen, D.J.J., Amaru, M.L., Torsvik, T.H.

792   (2010) Towards absolute plate motions constrained by lower-mantle slab

793   remnants. Nature Geoscience, 3, 36–40.

794   Vanpeteghem, C.B., Ohtani, E., and Kondo, T. (2002) Equation of state of the hydrous

795   phase δ-AlOOH at room temperature up to 22.5 GPa. Geophysical Research

796   Letters, 29, 1119.

797   Walter, M.J., Thomson, A.R., Wang, W., Lord, O.T., Ross, J., McMahon, S.C., Baron,

798   M.A., Melekhova, E., Kleppe, A.K., and Kohn, S.C. (2015) The stability of

799   hydrous silicates in Earth's lower mantle: experimental constraints from the

35

800   systems $MgO–SiO_2–H_2O$ and $MgO–Al_2O_3–SiO_2–H_2O$. Chemcal Geology, 418,

801   16–29.

802   Wirth, R., Vollmer, C., Brenker, F., Matsyuk, S., and Kaminsky, F. (2007) Inclusions of

803   nanocrystalline hydrous aluminium silicate "Phase Egg" in superdeep diamonds

804   from Juina (Mato Grosso State, Brazil). Earth and Planetary Science Letters, 259,

805   384–399.

806   Wu, Y., Wu, X., Lin, L.-F., McCammon, C.A., Xiao, Y., Chow, P., Prakapenka, V.B.,

807   Yoshino, T., Zhai, S., and Qin, S. (2016) Spin transition of ferric iron in the NAL

808   phase: Implications for the seismic heterogeneities of subducted slabs in the lower

809   mantle. Earth and Planetary Science Letters, 434, 91–100.

810   Xue, X., and Kanzaki, M. (2007) High-pressure $δ-Al(OH)_3$ and $δ-AlOOH$ phases and

811   isostructural hydroxides/oxyhydroxides: New structural insights from high-

812   resolution ^{1}H and ^{27}Al NMR. The Journal of physical Chemistry B, 111, 13156–

813   13166.

814

815   **FIGURE CAPTIONS**

816   **Figure 1.** One dimensional XRD patterns of δ-Fe12 (Run# DAF01) acquired at 12.3 and

817   44.0 GPa. The patterns were obtained during compression. Legend: δ, δ-phase (δ-Fe12);

818   He, solid helium (pressure medium); Re, rhenium (gasket material). $λ$ indicates the

819   wavelength of the X-rays. The uncertainty of $λ$ is given in parenthesis for the last reported

820   significant digit.

821

36

822   **Figure 2.** *P-V* profiles of δ-(Al,Fe)OOH (δ-Fe12, δ-Fe5, Fe-free δ-AlOOH). Blue circles

823   and light blue diamonds indicate the data of δ-Fe12 and δ-Fe5, respectively.

824   Experimental data for Fe-free δ-AlOOH are cited from Sano-Furukawa et al. (2009) (Red

825   squares, S09) and Kuribayashi et al. (2014) (purple triangles, K14). Solid and open

826   symbols indicate the data acquired during compression and decompression, respectively.

827   The uncertainties of pressure and volume are smaller than the symbols. In the case of the

828   data of Fe-free δ-AlOOH, only the data obtained in which helium was used as the

829   pressure medium were selected.

830

831   **Figure 3.** Axial ratios (left figures) and normalized lattice constants (right figures) as a

832   function of pressure for δ-(Al,Fe)OOH (δ-Fe12, δ-Fe5, Fe-free δ-AlOOH). Blue circles

833   and light blue diamonds indicate the data of δ-Fe12 and δ-Fe5, respectively. The

834   experimental data for Fe-free δ-AlOOH are cited from Sano-Furukawa et al. (2009) (Red

835   squares, S09) and Kuribayashi et al. (2014) (purple triangles, K14). In the case of the data

836   of Fe-free δ-AlOOH, only the data obtained in which helium was used as the pressure

837   medium were selected. To calculate the normalized lattice constants of δ-Fe12 and δ-Fe5,

838   the ambient pressure lattice constants of a δ-(Al$_{0.807(7)}$^{57}Fe$_{0.117(4)}$)OOH$_{1.15(3)}$ sample (the

839   CIF file is in the deposit), having an identical Fe/(Al+Fe) ratio to the δ-Fe12 sample

840   within error, were used for δ-Fe12 data (a_0 = 4.7458(13) Å, b_0 = 4.2564(11) Å, c_0 =

841   2.8519(6) Å), and those of δ-Fe5 which were measured at BL10XU after decompression

842   were used for δ-Fe5 data (a_0 = 4.7266(7) Å , b_0 = 4.2389(10) Å, c_0 = 2.8401(3) Å).

843

37

844   **Figure 4.** The *f-F* plots of δ-(Al,Fe)OOH (δ-Fe12, δ-Fe5, Fe-free δ-AlOOH) based on

845   data from this study, Sano-Furukawa et al. (2009) (S09), and Kuribayashi et al. (2014)

846   (K14). For δ-Fe12 and δ-Fe5, the V_0 obtained from 2nd BM EoS fits for the $P2_1nm$

847   structures were used in their plots (Table 3). The decrease or constant value in *F* between

848   *f* = 0 and ~0.02 are observed in all the data. The kink at ~10 GPa (*f* = ~0.02) in the *f-F*

849   plots corresponds to the change in axial compressibility, suggesting that the δ-

850   (Al,Fe)OOH phases could be classified into two structures with different compressibility

851   with boundary of 10 GPa. The decrease in *F* between 32 and 40 GPa (*f* = ~0.05–0.06) is

852   seen only in the data for the Fe-bearing δ-phases, which results from the spin transition of

853   Fe^{3+}.

854

855   **Figure 5.** *P-V* profiles with the fitted spin crossover EoS for δ-Fe12 (blue circles with a

856   gray line) and δ-Fe5 (light blue diamonds with a light gray line). The lines are spin

857   crossover EoS fitted with the MINUTI software (Sturhahn 2018). The inset indicates the

858   normalized residuals of fitting with 1σ error bars. The uncertainties of pressure and

859   volume are smaller than the symbols, and those of the spin transition pressure values are

860   given in parentheses for the last reported significant digit.

861

862   **Figure 6.** Isothermal bulk modulus (K_T), density (ρ), bulk sound velocity (v_Φ), the ratio of

863   ρ and v_Φ, and their uncertainties as a function of pressure for δ-Fe12 and δ-Fe5, resulting

864   from the spin crossover EoS fitted with MINUTI software (Sturhahn 2018). The EoS

865   parameters and fitting curves are shown in Table 3 and Fig. 5, respectively. The error for

866   each parameter is indicated by the gray area.

867

868   **Figure 7.** Synchrotron Mössbauer spectra of δ-Fe13 at six pressure conditions, without

869   the stainless steel reference foil (blue) and with the stainless steel (SS) foil (orange) in the

870   X-ray beam path, and their corresponding best fits (solid lines). The fitted hyperfine

871   parameters are given in Table 4. The reduced χ^2 for each dual fit is shown in the lower

872   left corner. The uncertainties of pressure are given in parentheses for the last reported

873   significant digit.

874

875   **Figure 8.** Quadrupole splitting and isomer shift (relative to α-Fe) of δ-Fe13. Orange

876   squares correspond to a high-spin Fe^{3+}-like site, dark blue circles are a low-spin Fe^{3+}_A site

877   with a low quadrupole splitting, and light blue diamonds are a low-spin Fe^{3+}_B site with an

878   intermediate quadrupole splitting. See Table 4 for tabulated hyperfine parameters.

879

880   **Figure 9.** (a) Isothermal bulk modulus, (b) density, (c) bulk sound velocity, and (d) the

881   ratio of density and bulk sound velocity as a function of pressure for δ-Fe12 (blue solid

882   line), δ-Fe5 (light blue solid line), δ-AlOOH (red dash-dot line), $MgSiO_4H_2$ Phase H

883   (green dash-dot line), ε-FeOOH (brown dotted line), and Fe-bearing NAL phase having a

884   chemical composition of $Na_{0.71}Mg_{2.05}Al_{4.62}Si_{1.16}Fe^{2+}_{0.09}Fe^{3+}_{0.17}O_{12}$ (orange dash-dot line).

885   PREM (Dziewonski and Anderson 1981) values are also shown for reference in (b)–(d)

886   (black dash line). The red dash-dot lines for δ-AlOOH with *Pnnm* structure are obtained

887   from the 3rd-order BM EoS fitting with MINUTI software (Sturhahn 2018), using the

888   pressure-volume dataset at the room temperature and pressures higher than 20 GPa

889   reported in both Sano-Furukawa et al. (2009) and Duan et al. (2018). The green dash-dot

39

890   lines for Phase H and the brown dotted lines for ε-FeOOH are reproduced with the 2nd or

891   3rd EoS parameters reported in Nishi et al. (2018) and Thompson et al. (2017),

892   respectively. The orange dash-dot lines indicate the data of Fe-bearing NAL phase, which

893   are determined by re-fitting for the *P-V* data of this phase (Wu et al. 2016) using MINUTI

894   software to obtain fit parameter error correlations and a consistency in the comparison of

895   trends. Solid and dash-dot lines are based on the experimental data at 300 K reported in

896   this study and the previous studies, while the dotted lines are based on theory at 0 K. The

897   errors for the data of δ-Fe12 and δ-Fe5 are only shown in Figure 6 to prevent the error

898   bars from overlapping with the other lines in this figure.

899

900   **Table 1.** Lattice constants and unit cell volumes determined for δ-Fe12, δ-

901    $(Al_{0.832(5)}{}^{57}Fe_{0.117(1)})OOH_{1.15(3)}$ (Fe/(Al+Fe) = 0.123(2)).

P_W (GPa)	P_{ruby} (GPa)	a (Å)	b (Å)	c (Å)	V (Å³)
Compression					
1.07(1)		4.7401(4)	4.2488(8)	2.8522(2)	57.44(3)
2.01(5)	1.62(8)	4.7301(3)	4.2376(5)	2.8486(1)	57.10(2)
4.65(3)	4.18(11)	4.7048(4)	4.2062(6)	2.8379(2)	56.16(2)
6.00(2)	5.54(15)	4.6919(3)	4.1920(5)	2.8321(2)	55.70(2)
7.71(5)		4.6781(4)	4.1725(5)	2.8256(2)	55.15(3)
7.83(2)		4.6762(5)	4.1711(6)	2.8248(2)	55.10(3)
10.13(6)	9.49(25)	4.6591(2)	4.1520(4)	2.8154(1)	54.46(2)
12.29(11)	11.86(1)	4.6456(4)	4.1403(6)	2.8075(2)	54.00(3)
17.38(5)	16.57(33)	4.6148(2)	4.1147(3)	2.7884(1)	52.95(1)
20.96(6)		4.5951(4)	4.0971(7)	2.7753(2)	52.24(3)
24.47(4)	23.76(30)	4.5763(2)	4.0832(3)	2.7637(1)	51.64(1)
28.62(3)	27.79(29)	4.5565(2)	4.0662(4)	2.7503(1)	50.96(2)
32.67(9)	31.73(22)	4.5373(4)	4.0532(8)	2.7379(3)	50.35(3)
37.93(15)		4.4967(5)	4.0170(8)	2.7104(3)	48.96(3)
40.83(49)		4.4840(6)	4.0065(7)	2.7002(3)	48.51(3)
44.03(58)		4.4703(7)	3.9936(9)	2.6901(4)	48.02(4)
46.88(45)		4.4602(9)	3.9852(18)	2.6829(4)	47.69(7)
50.85(33)		4.4455(10)	3.9750(20)	2.6742(5)	47.26(8)

40

53.80(35)	4.4351(17)	3.9663(25)	2.6678(7)	46.93(11)
58.27(34)	4.4205(15)	3.9536(22)	2.6568(6)	46.43(9)
62.04(33)	4.4094(9)	3.9434(13)	2.6500(3)	46.08(5)
64.83(35)	4.4009(15)	3.9394(18)	2.6427(6)	45.82(8)
Decompression				
53.97(6)	4.4405(11)	3.9684(15)	2.6704(6)	47.06(7)
47.17(7)	4.4607(6)	3.9851(8)	2.6845(4)	47.72(4)
44.23(11)	4.4707(6)	3.9940(7)	2.6913(4)	48.06(4)
42.06(20)	4.4799(5)	4.0018(8)	2.6974(3)	48.36(3)
37.02(26)	4.5046(3)	4.0255(5)	2.7156(2)	49.24(2)
35.22(28)	4.5222(5)	4.0397(7)	2.7267(2)	49.81(3)
33.16(26)	4.5328(6)	4.0492(9)	2.7334(3)	50.17(4)
32.14(10)	4.5444(6)	4.0556(12)	2.7398(4)	50.50(5)
29.79(5)	4.5586(4)	4.0660(7)	2.7498(2)	50.97(3)

902

903   P_W and P_{ruby} indicate the pressure values determined using the EoS for tungsten

904   (Dorogokupets and Oganov 2006) which are used as the experimental pressure, and the

905   ruby fluorescence method (Dewaele et al. 2008), respectively. Uncertainties are given in

906   parentheses for the last reported significant digit.

907

908

909

910

911

912

913

914

915

916

917

41

918

919

920

921

922

923

924

925

926

927

928 **Table 2.** Lattice constants and unit cell volumes determined for δ-Fe5 (δ-

929 $(Al_{0.908(9)}{}^{57}Fe_{0.045(1)})OOH_{1.14(3)}$ (Fe/(Al+Fe) = 0.047(10)).

P_W (GPa)	P_{ruby} (GPa)	a (Å)	b (Å)	c (Å)	V (Å^3)
Compression					
2.04(4)		4.7105(3)	4.2200(5)	2.8343(2)	56.34(2)
3.44(14)		4.6946(2)	4.2021(3)	2.8279(1)	55.79(1)
5.50(11)		4.6778(2)	4.1816(4)	2.8207(1)	55.17(2)
8.36(11)	7.73(14)	4.6515(3)	4.1490(4)	2.8091(1)	54.21(2)
12.36(18)		4.6244(2)	4.1244(3)	2.7934(1)	53.28(1)
13.67(30)	12.96(6)	4.6163(2)	4.1171(3)	2.7883(1)	52.99(2)
18.57(11)		4.5873(1)	4.0932(1)	2.7702(0)	52.02(1)
20.82(31)		4.5758(2)	4.0838(3)	2.7628(1)	51.63(1)
22.76(17)		4.5647(3)	4.0751(5)	2.7558(2)	51.26(2)
24.35(25)		4.557(2)	4.0698(4)	2.7511(1)	51.03(2)
25.63(56)	25.68(32)	4.5487(2)	4.0615(4)	2.7458(1)	50.73(2)
34.99(22)		4.5044(4)	4.0248(6)	2.7173(2)	49.26(3)
35.46(9)		4.5030(5)	4.0243(8)	2.7161(3)	49.22(3)
35.80(23)		4.4987(4)	4.0207(7)	2.7135(2)	49.08(3)
37.10(10)		4.4919(4)	4.0149(7)	2.7089(2)	48.85(3)
37.62(34)		4.4893(5)	4.0116(7)	2.7065(2)	48.74(3)
39.51(29)		4.4799(6)	4.0048(9)	2.7003(3)	48.45(4)
40.34(29)		4.4767(6)	4.0016(10)	2.6982(3)	48.34(4)

42

42.68(63)	4.4680(5)	3.9945(6)	2.6925(2)	48.05(3)
45.91(37)	4.4548(8)	3.9844(12)	2.6839(4)	47.64(5)
49.31(38)	4.4423(9)	3.9747(17)	2.6748(4)	47.23(7)
52.52(17)	4.4296(11)	3.9670(16)	2.6673(4)	46.87(7)
55.60(16)	4.4211(9)	3.9555(18)	2.6601(4)	46.52(7)
Decompression				
38.27(41)	4.4863(5)	4.0095(6)	2.7025(3)	48.61(3)
36.98(14)	4.4910(7)	4.0150(8)	2.7061(4)	48.80(4)
36.06(15)	4.4994(5)	4.0203(8)	2.7120(6)	49.06(4)
35.23(13)	4.5028(4)	4.0229(7)	2.7140(3)	49.16(3)
34.13(12)	4.5117(6)	4.0293(10)	2.7187(4)	49.42(4)
31.65(7)	4.5228(4)	4.0398(6)	2.7266(2)	49.82(3)
29.08(23)	4.5339(2)	4.0510(3)	2.7361(1)	50.25(2)
0.0001	4.7266(7)	4.2389(10)	2.8401(3)	56.90(5)

930

931   P_W and P_{ruby} indicate the pressure values determined using the EoS for tungsten

932   (Dorogokupets and Oganov 2006) which are used as the experimental pressure, and the

933   ruby fluorescence method (Dewaele et al. 2008), respectively. Uncertainties are given in

934   parentheses for the last reported significant digit.

935

936

937

938

939

940

941

942

943

944

945

43

946

947

948

949

950

951

952

953

954

955

956 **Table 3.** EoS Parameters of δ-(Al,Fe)OOH phases.

Phase	V_0 (Å³)	K_0 (GPa)	K' (GPa)	EoS	P range	Details
This study						
δ-($Al_{0.832(5)}$$^{57}Fe_{0.117(1)}$)$OOH_{1.15(3)}$	57.85(2)	147(1)	4 (fixed)	2nd BM	1.0–10.1 GPa	δ-Fe12 (Fe/(Al+Fe) = 0.123(2)), $P2_1nm$, HS
δ-($Al_{0.832(5)}$$^{57}Fe_{0.117(1)}$)$OOH_{1.15(3)}$	57.5(3)	155(22)	8(2)	Spin crossover EoS	10.1–64.8 GPa	δ-Fe12 (Fe/(Al+Fe) = 0.123(2)), $Pnnm$, HS
δ-($Al_{0.832(5)}$$^{57}Fe_{0.117(1)}$)$OOH_{1.15(3)}$	55.2(4)	241(14)	4 (fixed)	Spin crossover EoS		δ-Fe12 (Fe/(Al+Fe) = 0.123(2)), $Pnnm$, LS
δ-($Al_{0.908(9)}$$^{57}Fe_{0.045(1)}$)$OOH_{1.14(3)}$	57.03(7)	152(7)	4 (fixed)	2nd BM	0–8.4 GPa	δ-Fe5 (Fe/(Al+Fe) = 0.047(10)), $P2_1nm$, HS
δ-($Al_{0.908(9)}$$^{57}Fe_{0.045(1)}$)$OOH_{1.14(3)}$	56.9(4)	149(25)	8(2)	Spin crossover EoS	12.4–55.6 GPa	δ-Fe5 (Fe/(Al+Fe) = 0.047(10)), $Pnnm$, HS
δ-($Al_{0.908(9)}$$^{57}Fe_{0.045(1)}$)$OOH_{1.14(3)}$	55.4(3)	223(11)	4 (fixed)	Spin crossover EoS		δ-Fe5 (Fe/(Al+Fe) = 0.047(10)), $Pnnm$, LS
Previous study						References
δ-AlOOH	56.408(9)	152(2)	4 (fixed)	2nd BM	0–10 GPa	Sano-Furukawa et al. (2009)
δ-AlOOH	55.47(8)	219(3)	4 (fixed)	2nd BM	10–63.5 GPa	Sano-Furukawa et al. (2009)
δ-AlOOH	56.408(9)	191(1)	4 (fixed)	2nd BM	0–63.5 GPa	Sano-Furukawa et al. (2009)
δ-AlOOH	56.408(9)	162(3)	5.9(2)	3rd BM	0–63.5 GPa	Sano-Furukawa et al. (2009)
δ-AlOOH	56.54(9)	252(3)	4 (fixed)	3rd BM	0–22.5 GPa	Vanpeteghem et al. (2002)
δ-AlOOH	56.35(2)	124(2)	13.5(7)	3rd BM	0–17.1 GPa	Suzuki (2009)
δ-AlOOH[a]	167	167	5.0	Vinet	0–28 GPa	Tsuchiya and Tsuchiya (2009)
δ-AlOOH[b]	57.57	205	4.3	Vinet	0–150 GPa	Tsuchiya and Tsuchiya (2009)
ε-FeOOH[c]	66.3(5)	158(5)	4 (fixed)	2nd BM	0–21 GPa	Gleason et al. (2008)
ε-FeOOH	66.20(3)	126(3)	10(1)	3rd BM	0–8.6 GPa	Suzuki (2010)
ε-FeOOH	66.278(6)	135(3)	6.1(9)	3rd BM	0–11.1 GPa	Suzuki (2016)

44

ε-FeOOH[d]	58.62(2)	223(2)	4.07(3)	3rd BM	30–140 GPa	Thompson et al. (2017)

957

958   Uncertainties are given in parentheses for the last reported significant digit.

959   HS, high-spin state; LS, low-spin state

960   a, Theory, $P2_1nm$ structure.

961   b, Theory, $Pnnm$ (HC) structure.

962   c, Experimental data were obtained at 473–673 K.

963   d, Theory, $Pnnm$ (HC) structure and low-spin state.

964

965

966   **Table 4.** Hyperfine parameters for δ-Fe13 and the corresponding reduced χ^2 produced

967   from fitting the spectra of the sample with and without the stainless steel reference foil

968   simultaneously. Uncertainties are given in parentheses for the last reported significant

969   digit. Isomer shifts are relative to α-Fe metal. In low-spin δ-Fe13, $Fe^{3+}_B/(Fe^{3+}_A + Fe^{3+}_B)$

970   was found to be 1/3 through Monte-Carlo searches and did not change with pressure, and

971   so was fixed to reduce parameter correlations. See text for more details.

HS

Pressure (GPa)	QS (mm/s)	IS (mm/s)	FWHM (mm/s)	Thickness (μm)	reduced χ^2
21.1(2)	0.414(7)	0.19(2)	0.12(1)	23.8(5)	1.36(6)
31.8(8)	0.392(3)	0.18(2)	0.01(5)	26.4(2)	1.88(7)

LS

Pressure (GPa)	QS_A (mm/s)	IS_A (mm/s)	$FWHM_A$ (mm/s)	QS_B (mm/s)	IS_B (mm/s)	$FWHM_B$ (mm/s)	Thickness (μm)	reduced χ^2
45(2)	1.140(4)	0.209(7)	0.260(4)	1.73(1)	0.249(7)	0.16(1)	19.8(5)	1.23(5)
59(2)	1.235(6)	0.135(8)	0.221(5)	1.864(7)	0.206(9)	0.22(1)	18.0(4)	1.12(5)
67.5(5)	1.291(6)	0.107(6)	0.215(4)	1.88(1)	0.172(9)	0.28(2)	16.9(2)	1.50(6)
78.5(5)	1.320(6)	0.109(7)	0.227(4)	2.006(9)	0.202(9)	0.28(2)	16.1(2)	1.61(6)

972

973

45

974   **Table 5.** Euler angles α and β for the electric field gradient orientation of high-spin (HS)

975   and low-spin (LS) ferric iron sites in δ-Fe13.

	α	β
HS Fe^{3+}	0°	0°
LS Fe$^{3+}_A$	296°	261°
LS Fe$^{3+}_B$	22°	253°

976

977

Figure 1
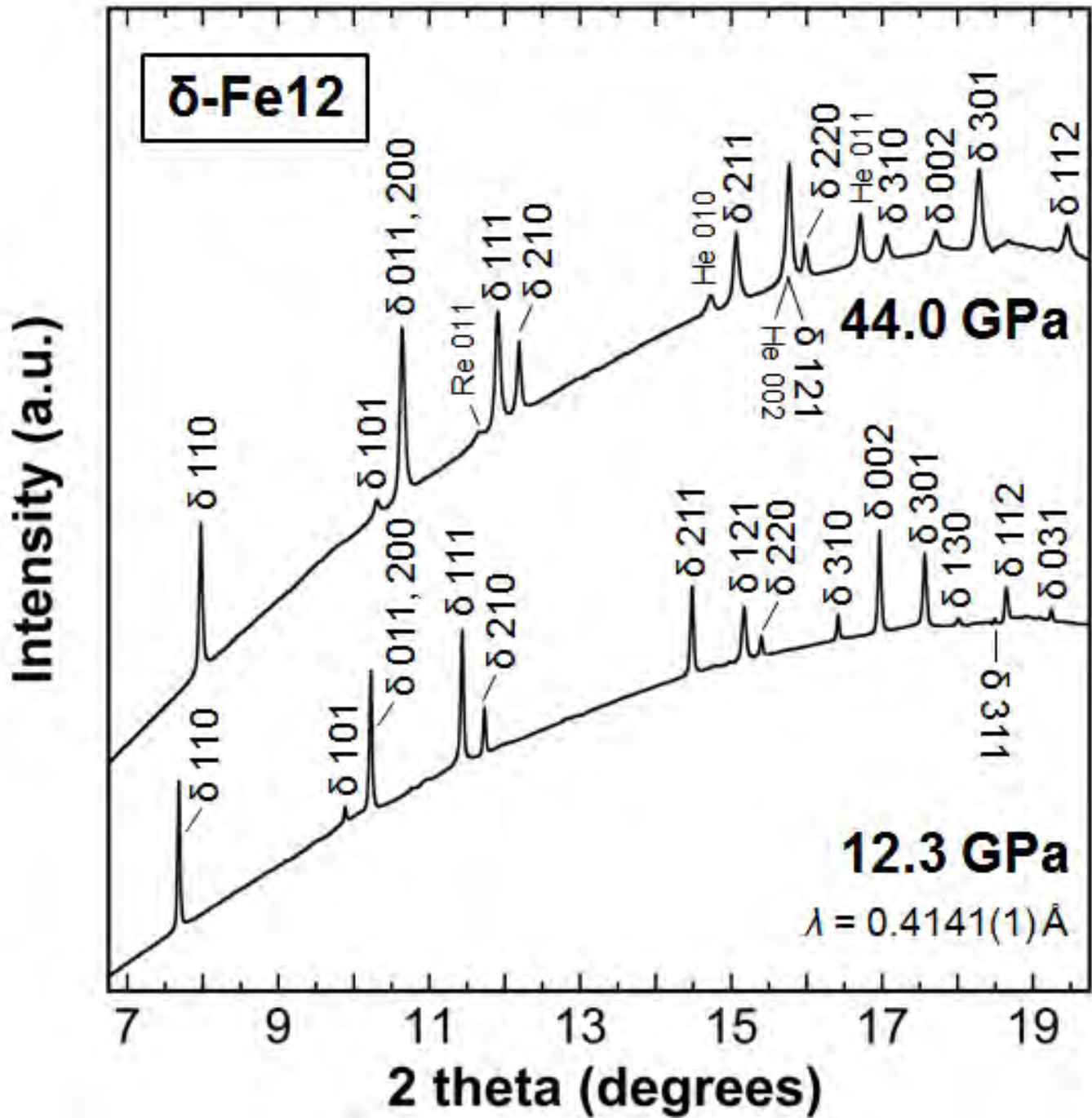
Figure 2
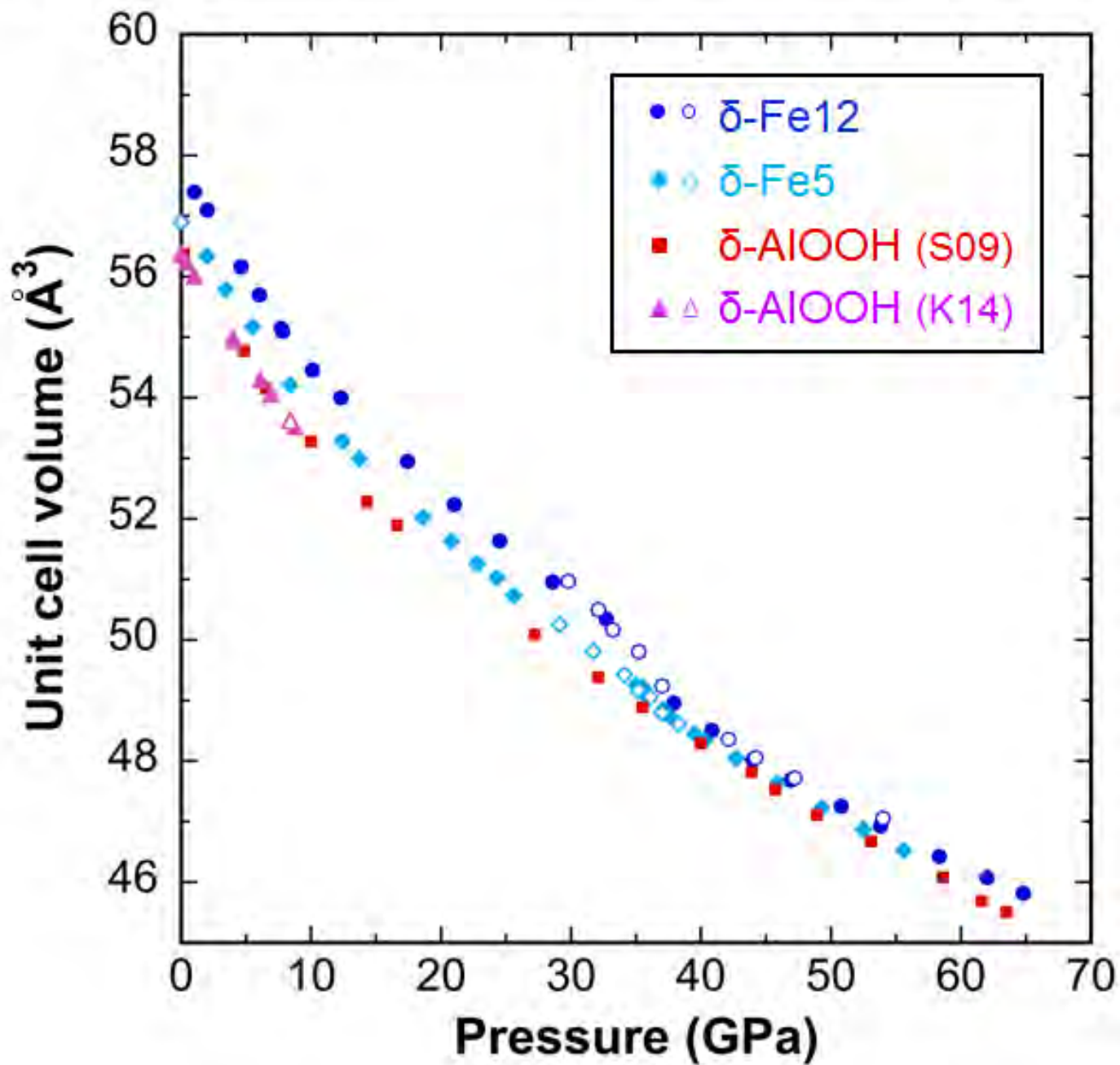
Figure 3
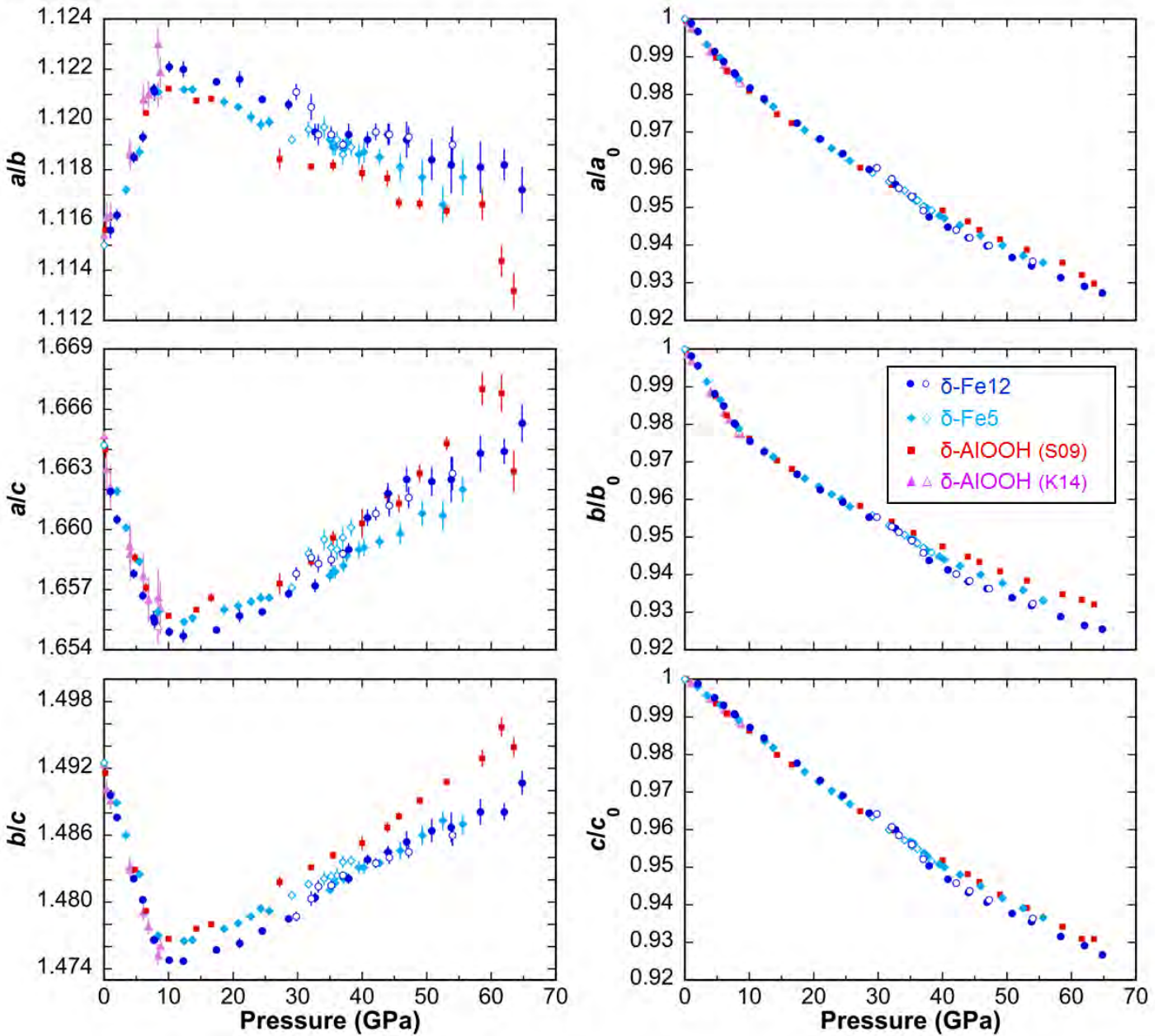
Figure 4
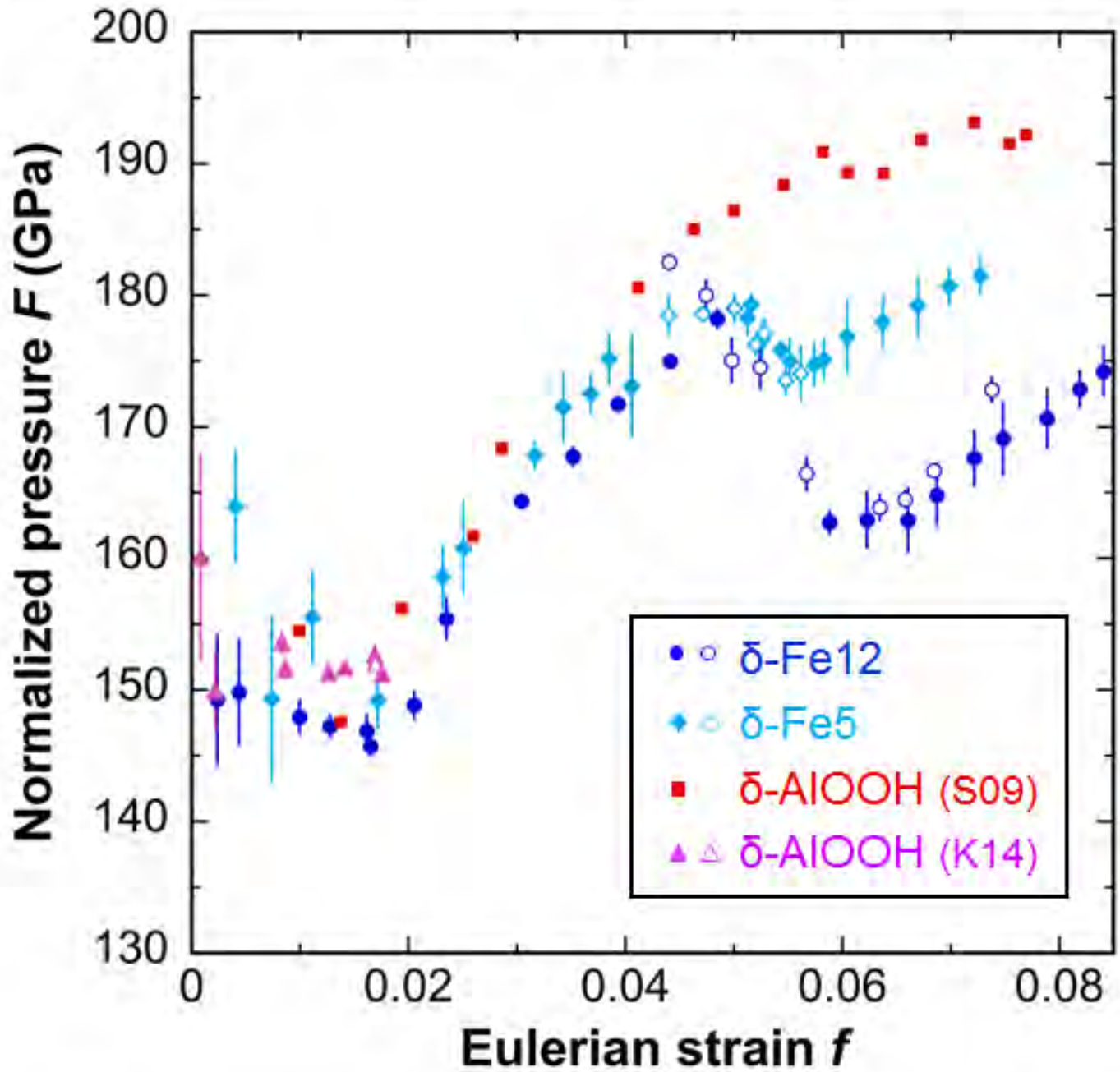
Figure 5
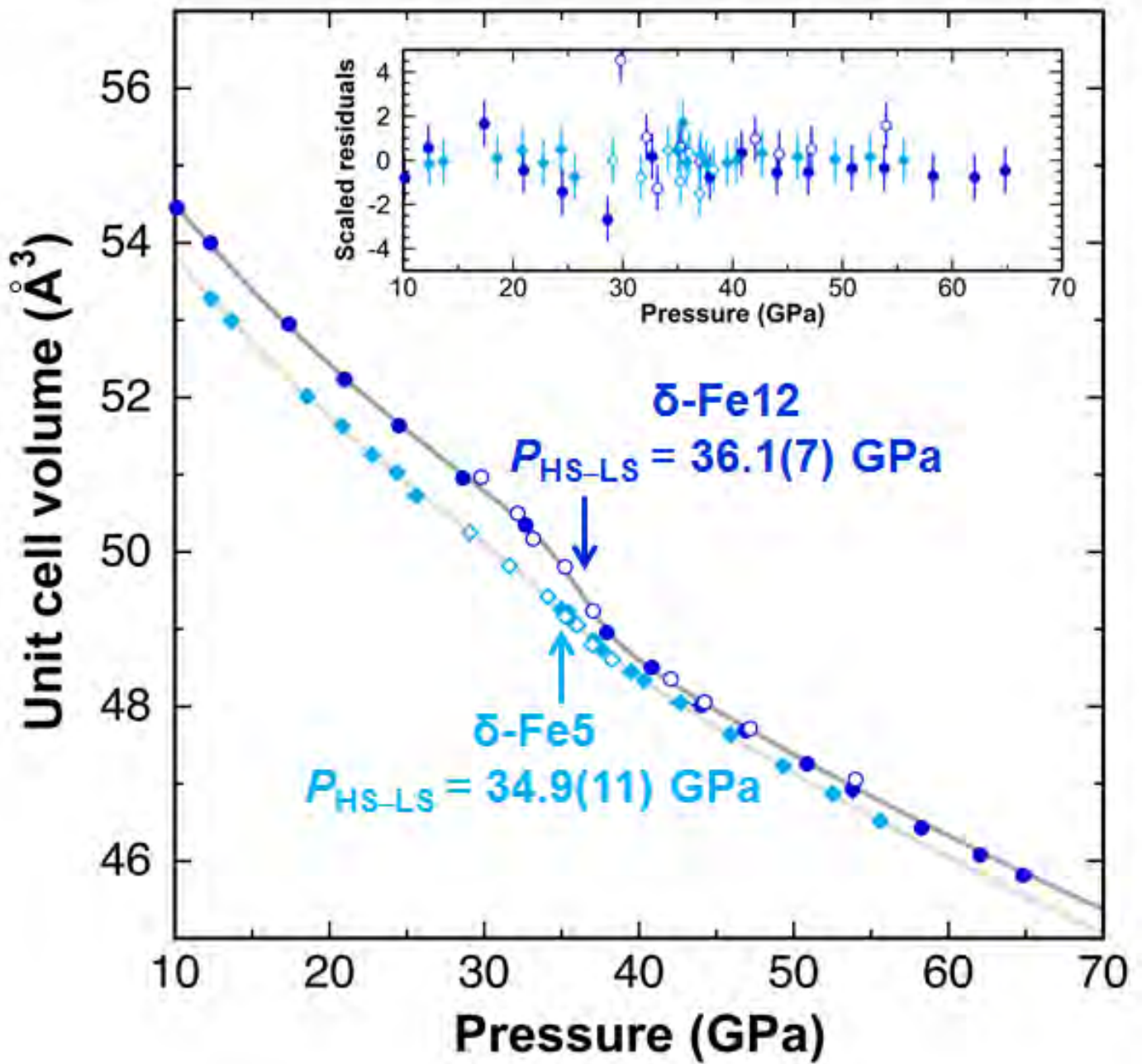
Figure 6

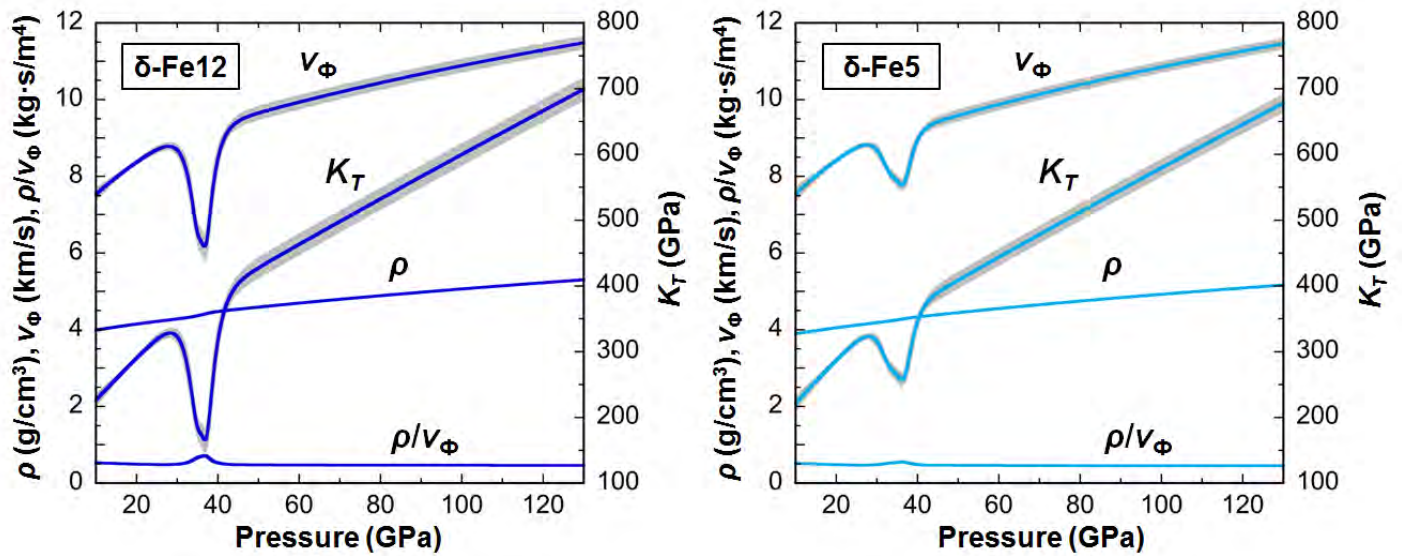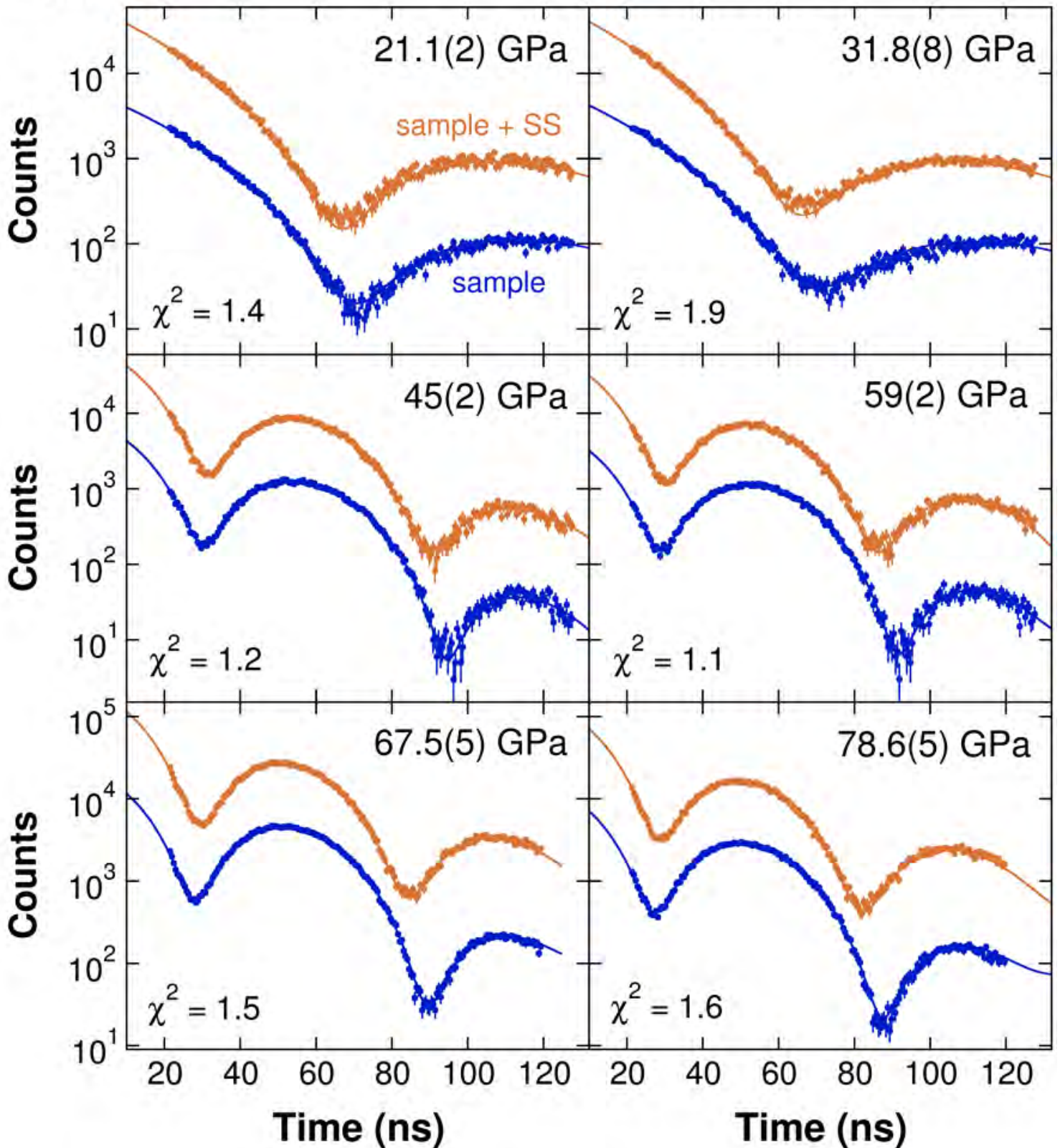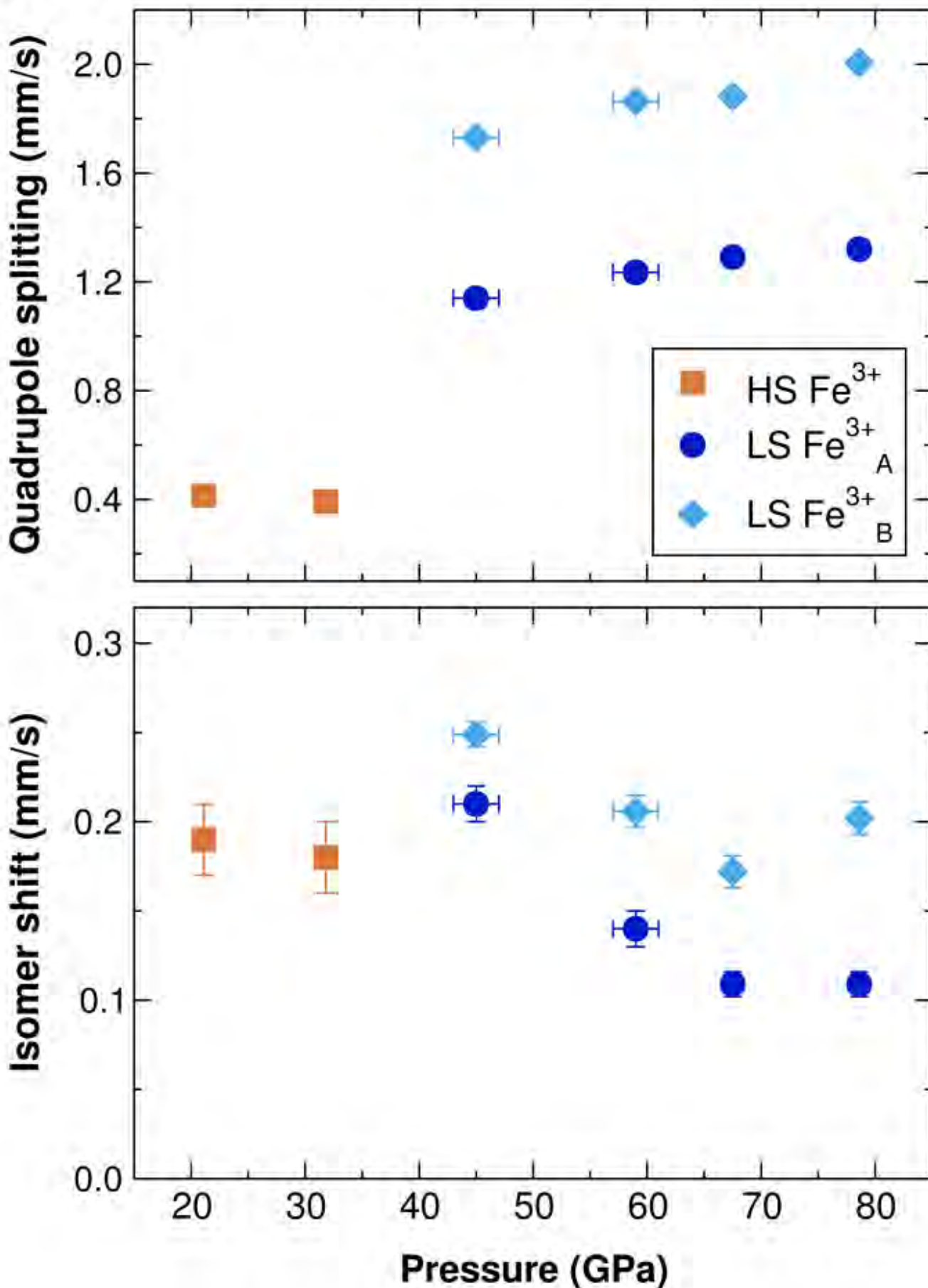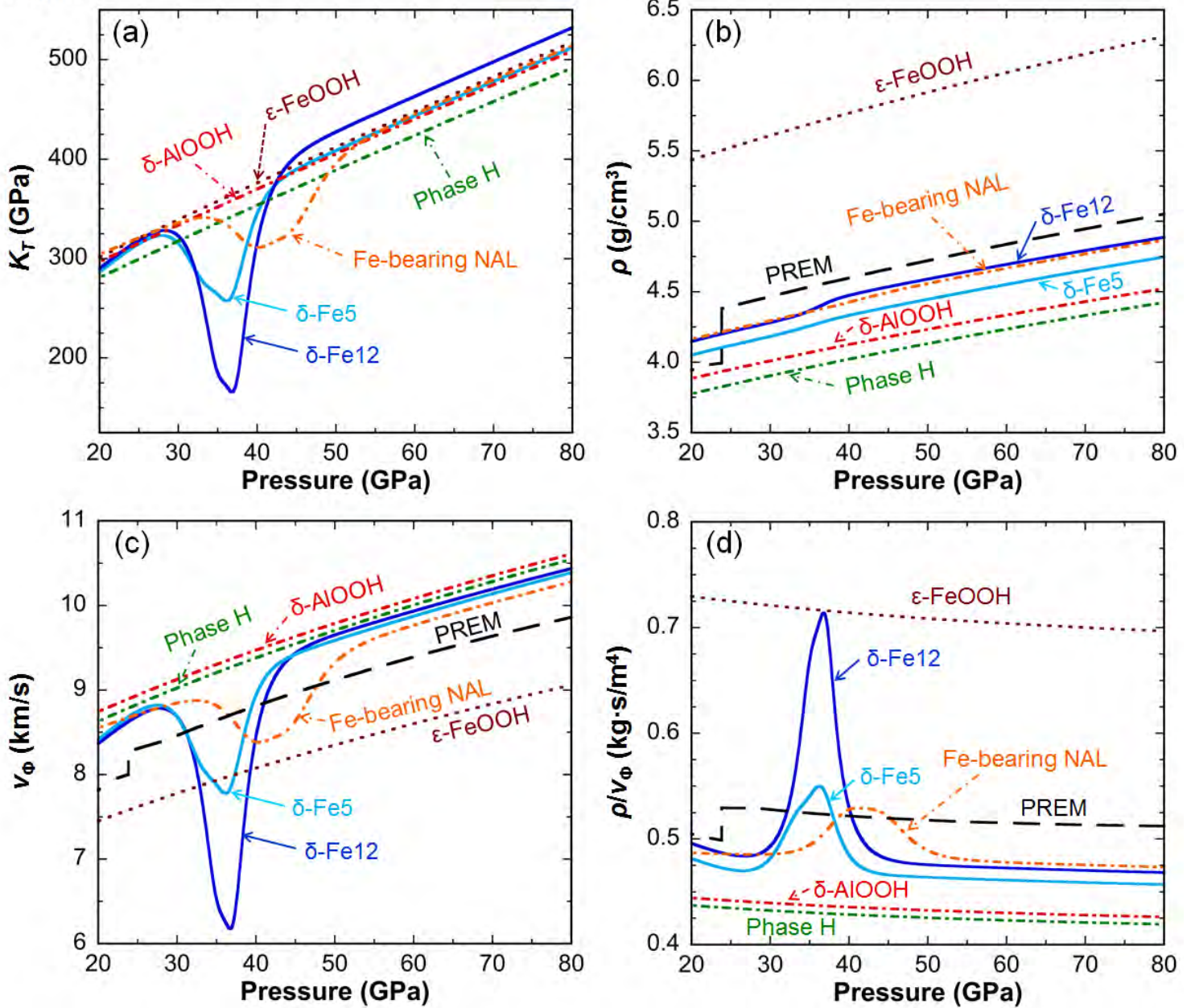**Figure 7**

Figure 8

Figure 9

Table 1. Lattice constants and unit cell volumes determined for δ-Fe12, δ-(Al$_{0.832(5)}$^{57}Fe$_{0.117(1)}$)OOH$_{1.15(3)}$ (Fe/(Al+Fe) = 0.123(

P_W (GPa)	P_{ruby} (GPa)	a (Å)	b (Å)	c (Å)	V (Å^3)
Compression					
1.07(1)		4.7401(4)	4.2488(8)	2.8522(2)	57.44(3)
2.01(5)	1.62(8)	4.7301(3)	4.2376(5)	2.8486(1)	57.10(2)
4.65(3)	4.18(11)	4.7048(4)	4.2062(6)	2.8379(2)	56.16(2)
6.00(2)	5.54(15)	4.6919(3)	4.1920(5)	2.8321(2)	55.70(2)
7.71(5)		4.6781(4)	4.1725(5)	2.8256(2)	55.15(3)
7.83(2)		4.6762(5)	4.1711(6)	2.8248(2)	55.10(3)
10.13(6)	9.49(25)	4.6591(2)	4.1520(4)	2.8154(1)	54.46(2)
12.29(11)	11.86(1)	4.6456(4)	4.1403(6)	2.8075(2)	54.00(3)
17.38(5)	16.57(33)	4.6148(2)	4.1147(3)	2.7884(1)	52.95(1)
20.96(6)		4.5951(4)	4.0971(7)	2.7753(2)	52.24(3)
24.47(4)	23.76(30)	4.5763(2)	4.0832(3)	2.7637(1)	51.64(1)
28.62(3)	27.79(29)	4.5565(2)	4.0662(4)	2.7503(1)	50.96(2)
32.67(9)	31.73(22)	4.5373(4)	4.0532(8)	2.7379(3)	50.35(3)
37.93(15)		4.4967(5)	4.0170(8)	2.7104(3)	48.96(3)
40.83(49)		4.4840(6)	4.0065(7)	2.7002(3)	48.51(3)
44.03(58)		4.4703(7)	3.9936(9)	2.6901(4)	48.02(4)
46.88(45)		4.4602(9)	3.9852(18)	2.6829(4)	47.69(7)
50.85(33)		4.4455(10)	3.9750(20)	2.6742(5)	47.26(8)
53.80(35)		4.4351(17)	3.9663(25)	2.6678(7)	46.93(11)
58.27(34)		4.4205(15)	3.9536(22)	2.6568(6)	46.43(9)
62.04(33)		4.4094(9)	3.9434(13)	2.6500(3)	46.08(5)
64.83(35)		4.4009(15)	3.9394(18)	2.6427(6)	45.82(8)
Decompression					
53.97(6)		4.4405(11)	3.9684(15)	2.6704(6)	47.06(7)
47.17(7)		4.4607(6)	3.9851(8)	2.6845(4)	47.72(4)
44.23(11)		4.4707(6)	3.9940(7)	2.6913(4)	48.06(4)
42.06(20)		4.4799(5)	4.0018(8)	2.6974(3)	48.36(3)
37.02(26)		4.5046(3)	4.0255(5)	2.7156(2)	49.24(2)
35.22(28)		4.5222(5)	4.0397(7)	2.7267(2)	49.81(3)
33.16(26)		4.5328(6)	4.0492(9)	2.7334(3)	50.17(4)
32.14(10)		4.5444(6)	4.0556(12)	2.7398(4)	50.50(5)
29.79(5)		4.5586(4)	4.0660(7)	2.7498(2)	50.97(3)

P_W and P_{ruby} indicate the pressure values determined using the EoS for tungsten (Dorogokupets and Oganov 2006) which are used as the experimental pressure, and the ruby fluorescence method (Dewaele et al. 2008), respectively. Uncertainties are given in parentheses for the last reported significant digit.

Table 2. Lattice constants and unit cell volumes determined for δ-Fe5 (δ-(Al$_{0.908(9)}$^{57}Fe$_{0.045(1)}$)OOH$_{1.14(3)}$ (Fe/(Al+Fe) = 0.047(1

P_W (GPa)	P_{ruby} (GPa)	a (Å)	b (Å)	c (Å)	V (Å^3)
Compression					
2.04(4)		4.7105(3)	4.2200(5)	2.8343(2)	56.34(2)
3.44(14)		4.6946(2)	4.2021(3)	2.8279(1)	55.79(1)
5.50(11)		4.6778(2)	4.1816(4)	2.8207(1)	55.17(2)
8.36(11)	7.73(14)	4.6515(3)	4.1490(4)	2.8091(1)	54.21(2)
12.36(18)		4.6244(2)	4.1244(3)	2.7934(1)	53.28(1)
13.67(30)	12.96(6)	4.6163(2)	4.1171(3)	2.7883(1)	52.99(2)
18.57(11)		4.5873(1)	4.0932(1)	2.7702(0)	52.02(1)
20.82(31)		4.5758(2)	4.0838(3)	2.7628(1)	51.63(1)
22.76(17)		4.5647(3)	4.0751(5)	2.7558(2)	51.26(2)
24.35(25)		4.557(2)	4.0698(4)	2.7511(1)	51.03(2)
25.63(56)	25.68(32)	4.5487(2)	4.0615(4)	2.7458(1)	50.73(2)
34.99(22)		4.5044(4)	4.0248(6)	2.7173(2)	49.26(3)
35.46(9)		4.5030(5)	4.0243(8)	2.7161(3)	49.22(3)
35.80(23)		4.4987(4)	4.0207(7)	2.7135(2)	49.08(3)
37.10(10)		4.4919(4)	4.0149(7)	2.7089(2)	48.85(3)
37.62(34)		4.4893(5)	4.0116(7)	2.7065(2)	48.74(3)
39.51(29)		4.4799(6)	4.0048(9)	2.7003(3)	48.45(4)
40.34(29)		4.4767(6)	4.0016(10)	2.6982(3)	48.34(4)
42.68(63)		4.4680(5)	3.9945(6)	2.6925(2)	48.05(3)
45.91(37)		4.4548(8)	3.9844(12)	2.6839(4)	47.64(5)
49.31(38)		4.4423(9)	3.9747(17)	2.6748(4)	47.23(7)
52.52(17)		4.4296(11)	3.9670(16)	2.6673(4)	46.87(7)
55.60(16)		4.4211(9)	3.9555(18)	2.6601(4)	46.52(7)
Decompression					
38.27(41)		4.4863(5)	4.0095(6)	2.7025(3)	48.61(3)
36.98(14)		4.4910(7)	4.0150(8)	2.7061(4)	48.80(4)
36.06(15)		4.4994(5)	4.0203(8)	2.7120(6)	49.06(4)
35.23(13)		4.5028(4)	4.0229(7)	2.7140(3)	49.16(3)
34.13(12)		4.5117(6)	4.0293(10)	2.7187(4)	49.42(4)
31.65(7)		4.5228(4)	4.0398(6)	2.7266(2)	49.82(3)
29.08(23)		4.5339(2)	4.0510(3)	2.7361(1)	50.25(2)
0.0001		4.7266(7)	4.2389(10)	2.8401(3)	56.90(5)

P_W and P_{ruby} indicate the pressure values determined using the EoS for tungsten (Dorogokupets and Oganov 2006) which are used as the experimental pressure, and the ruby fluorescence method (Dewaele et al. 2008), respectively. Uncertainties are given in parentheses for the last reported significant digit.

Table 3. EoS Parameters of δ-(Al,Fe)OOH phases.

Phase	V_0 (Å^3)	K_0 (GPa)	K' (GPa)	EoS	P range
This study					
δ-(Al$_{0.832(5)}$^{57}Fe$_{0.117(1)}$)OOH$_{1.15(3)}$	57.85(2)	147(1)	4 (fixed)	2nd BM	1.0–10.1 GPa
δ-(Al$_{0.832(5)}$^{57}Fe$_{0.117(1)}$)OOH$_{1.15(3)}$	57.5(3)	155(22)	8(2)	Spin crossover EoS	10.1–64.8 GPa
δ-(Al$_{0.832(5)}$^{57}Fe$_{0.117(1)}$)OOH$_{1.15(3)}$	55.2(4)	241(14)	4 (fixed)	Spin crossover EoS	
δ-(Al$_{0.908(9)}$^{57}Fe$_{0.045(1)}$)OOH$_{1.14(3)}$	57.03(7)	152(7)	4 (fixed)	2nd BM	0–8.4 GPa
δ-(Al$_{0.908(9)}$^{57}Fe$_{0.045(1)}$)OOH$_{1.14(3)}$	56.9(4)	149(25)	8(2)	Spin crossover EoS	12.4–55.6 GPa
δ-(Al$_{0.908(9)}$^{57}Fe$_{0.045(1)}$)OOH$_{1.14(3)}$	55.4(3)	223(11)	4 (fixed)	Spin crossover EoS	
Previous study					
δ-AlOOH	56.408(9)	152(2)	4 (fixed)	2nd BM	0–10 GPa
δ-AlOOH	55.47(8)	219(3)	4 (fixed)	2nd BM	10–63.5 GPa
δ-AlOOH	56.408(9)	191(1)	4 (fixed)	2nd BM	0–63.5 GPa
δ-AlOOH	56.408(9)	162(3)	5.9(2)	3rd BM	0–63.5 GPa
δ-AlOOH	56.54(9)	252(3)	4 (fixed)	3rd BM	0–22.5 GPa
δ-AlOOH	56.35(2)	124(2)	13.5(7)	3rd BM	0–17.1 GPa
δ-AlOOH[a]	167	167	5.0	Vinet	0–28 GPa
δ-AlOOH[b]	57.57	205	4.3	Vinet	0–150 GPa
ε-FeOOH[c]	66.3(5)	158(5)	4 (fixed)	2nd BM	0–21 GPa
ε-FeOOH	66.20(3)	126(3)	10(1)	3rd BM	0–8.6 GPa
ε-FeOOH	66.278(6)	135(3)	6.1(9)	3rd BM	0–11.1 GPa
ε-FeOOH[d]	58.62(2)	223(2)	4.07(3)	3rd BM	30–140 GPa

Uncertainties are given in parentheses for the last reported significant digit.

HS, high-spin state; LS, low-spin state

a, Theory, $P2_1nm$ structure.

b, Theory, $Pnnm$ (HC) structure.

c, Experimental data were obtained at 473-673 K.

d, Theory, $Pnnm$ (HC) structure and LS state.

Details

δ-Fe12 (Fe/(Al+Fe) = 0.123(2)), $P 2_1 nm$, HS

δ-Fe12 (Fe/(Al+Fe) = 0.123(2)), $Pnnm$, HS

δ-Fe12 (Fe/(Al+Fe) = 0.123(2)), $Pnnm$, LS

δ-Fe5 (Fe/(Al+Fe) = 0.047(10)), $P 2_1 nm$, HS

δ-Fe5 (Fe/(Al+Fe) = 0.047(10)), $Pnnm$, HS

δ-Fe5 (Fe/(Al+Fe) = 0.047(10)), $Pnnm$, LS

References

Sano-Furukawa et al. (2009)

Sano-Furukawa et al. (2009)

Sano-Furukawa et al. (2009)

Sano-Furukawa et al. (2009)

Vanpeteghem et al. (2002)

Suzuki (2009)

Tsuchiya and Tsuchiya (2009)

Tsuchiya and Tsuchiya (2009)

Gleason et al. (2008)

Suzuki (2010)

Suzuki (2016)

Thompson et al. (2017)

Table 4. Hyperfine parameters for δ-Fe13 and the corresponding reduced χ^2 produced from fitting the spectra of the sample w
reference foil simultaneously. Uncertainties are given in parentheses for the last reported significant digit. Isomer shifts are rel
Fe13, $Fe^{3+}_B/(Fe^{3+}_A + Fe^{3+}_B)$ was found to be 1/3 through Monte-Carlo searches and did not change with pressure, and so was f
correlations. See text for more details.

HS

Pressure (GPa)	QS (mm/s)	IS (mm/s)	FWHM (mm/s)	Thickness (μm)	reduced χ^2_r
21.1(2)	0.414(7)	0.19(2)	0.12(1)	23.8(5)	1.36(6)
31.8(8)	0.392(3)	0.18(2)	0.01(5)	26.4(2)	1.88(7)

LS

Pressure (GPa)	QS_A (mm/s)	IS_A (mm/s)	$FWHM_A$ (mm/s)	QS_B (mm/s)	IS_B (mm/s)	$FWHM_B$ (mm/s)
45(2)	1.140(4)	0.209(7)	0.260(4)	1.73(1)	0.249(7)	0.16(1)
59(2)	1.235(6)	0.135(8)	0.221(5)	1.864(7)	0.206(9)	0.22(1)
67.5(5)	1.291(6)	0.107(6)	0.215(4)	1.88(1)	0.172(9)	0.28(2)
78.5(5)	1.320(6)	0.109(7)	0.227(4)	2.006(9)	0.202(9)	0.28(2)

with and without the stainless steel
lative to α-Fe metal. In low-spin δ-
fixed to reduce parameter

Thickness (μm)	reduced χ^2
19.8(5)	1.23(5)
18.0(4)	1.12(5)
16.9(2)	1.50(6)
16.1(2)	1.61(6)

Table 5. Euler angles α and β for the electric field gradient orientation of high-spin (HS) and low-spin (LS) ferric iron sites

	α	β
HS Fe^{3+}	0°	0°
LS Fe^{3+}_A	296°	261°
LS Fe^{3+}_B	22°	253°

in δ-Fe13.